Kinetic Parameterization of the Effects of Atmospheric and Self-Generated Carbon Dioxide on the Thermal Decomposition of Calcium Carbonate

Mito Hotta, Taiga Tone, Loïc Favergeon, Nobuyoshi Koga

Kinetic Parameterization of the Effects of Atmospheric and Self-Generated Carbon Dioxide on the Thermal Decomposition of Calcium Carbonate

Mito Hotta,[1] Taiga Tone,[1] Loic Favergeon[2], and Nobuyoshi Koga,[1,]*

[1] Department of Science Education, Division of Educational Sciences, Graduate School of Humanities and Social Sciences, Hiroshima University, 1-1-1 Kagamiyama, Higashi-Hiroshima 739-8524, Japan.
[2] Mines Saint-Etienne, Univ. Lyon, CNRS, UMR 5307 LGF, Centre SPIN, F-42023 Saint-Etienne, France

Abstract
The kinetics of the thermal decomposition of $CaCO_3$ is significantly influenced by atmospheric and selfgenerated CO_2 due to the reversibility of the reaction. More detailed understanding of this well-known phenomenon is desired for establishing an effective Ca-looping in the CaO–$CaCO_3$ system for energy storage and CO_2 capture. This article shows the universal kinetics of the thermal decomposition of $CaCO_3$ over different temperatures and partial pressures of CO_2 ($p(CO_2)$) with the aid of an accommodation function (AF) composed of $p(CO_2)$ and equilibrium pressure. An analytical form of AF with exponents (a, b) was derived based on the kinetic considerations for the consecutive elementary steps of the surface nucleation and interfacial reaction. The overall kinetics of the thermal decomposition of $CaCO_3$ were described universally over different temperatures and $p(CO_2)$ values by introducing the AF, in views of the isoconversional and isothermal kinetic relationships using the extended Friedman and experimental master plots, respectively. The universal kinetic description was extended to the kinetic modeling based on the physico-geometrical consecutive process comprising induction period (IP), surface reaction (SR), and phase boundary-controlled reaction (PBR). The proposed kinetic approach enables parameterizing the CO_2 effect via the optimized (a, b) and to track changes in the CO_2 effect as the physico-geometrical reaction step advanced from IP to PBR via SR. Furthermore, using the established universal kinetic description across different temperatures and $p(CO_2)$ values, a challenge was set to quantify the contributions of atmospheric and self-generated CO_2 on the kinetics.

1. Introduction

Thermal decomposition of $CaCO_3$ is one of the most studied processes among other inorganic salts because of its potential applications for historical building materials and other industrial processes with a mine of natural resources as minerals and those produced by biomineralization.[1]

$$CaCO_3(s) \rightleftarrows CaO(s) + CO_2(g) \qquad (1)$$

The reversible nature of the reaction is a key functionality of this reaction system accompanied by release/adsorption of CO_2 and endothermic/exothermic changes, which has recently focused on establishing the most effective Ca-looping system for energy storage[2-11] and CO_2 capture[12-

[19] technologies. Kinetic behavior of the thermal decomposition of $CaCO_3$ is characterized by the significant effect of atmospheric CO_2.[20-30] Under linearly increasing temperature conditions at a fixed heating rate (β), thermogravimetry (TG)–derivative TG (DTG)–differential thermal analysis (DTA) curves for the thermal decomposition of $CaCO_3$ shift systematically to higher temperatures with increasing the partial pressure of CO_2 ($p(CO_2)$) in the reaction atmosphere (Figure 1), in which the shift of the reaction initiation temperature is more significant compared with that of the reaction ending temperature. Thus, the reaction temperature range under linear nonisothermal conditions decreases with increasing $p(CO_2)$ value, accompanied by the systematic increase in the peak heights of DTG and DTA curves. The reversible nature of the reaction explains the well-known thermal decomposition behavior of $CaCO_3$ under different $p(CO_2)$, which is considered typical behavior due to chemical equilibrium.20-30 In many previous kinetic studies, the thermal decomposition of $CaCO_3$ was analyzed using the kinetic equation with the single-step approximation and without considering the effect of $p(CO_2)$:[31-33]

$$\frac{d\alpha}{dt} = A\exp\left(-\frac{E_a}{RT}\right)f(\alpha), \qquad (2)$$

where α, A, E_a, and R are the fractional reaction, Arrhenius preexponential factor, apparent activation energy, and gas constant, respectively. The kinetic model function $f(\alpha)$ accommodates the variation of the reaction rate as the reaction advances and is derived by considering the reaction geometry and the linear advancement kinetics of the reaction interface.[34-36] Application of the kinetic equation (eq. (2)) to the thermal decomposition of $CaCO_3$ at different $p(CO_2)$ causes different linear correlations of the Arrhenius-type plots among the reactions at different $p(CO_2)$ values. The formal kinetic results based on eq. (2) are sensitive to the sampling and measurement conditions for tracking the thermal decomposition process due to changes in the mass transfer phenomena because the self-generated CO_2 contributes to the actual $p(CO_2)$ value that effects the kinetics.[29] This must be a reason for the large discrepancy of the kinetic results reported in previous publications.[37-38]

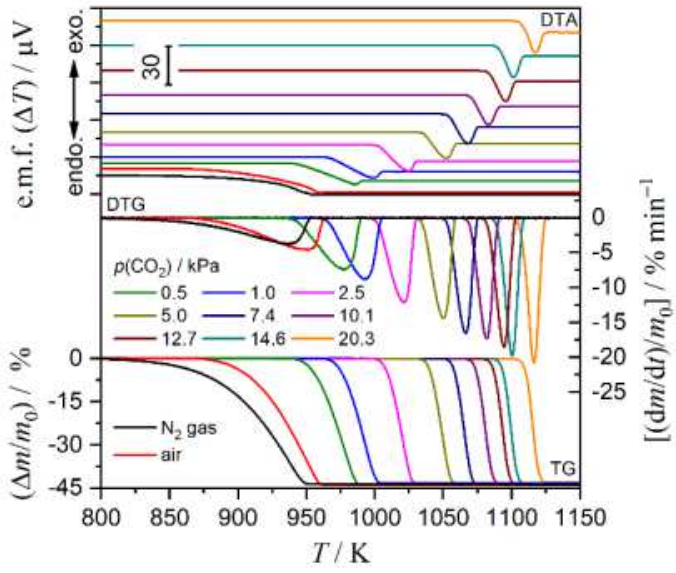

Figure 1. TG–DTG–DTA curves for the thermal decomposition of $CaCO_3$ (sample mass: m_0 = 2.523 ± 0.013 mg) recorded at a β of 5 K min^{-1} in a stream of dry N_2, air, or N_2–CO_2 mixed gases characterized by different $p(CO_2)$ values at a flow rate (q_v) of 300 cm^3 min^{-1}.

The introduction of an accommodation function (AF; $h(p(CO_2), P_{eq}(T))$) into the fundamental kinetic equation has been investigated for a rigorous kinetic description considering the influence of $p(CO_2)$.[21, 23-25, 39-43]

$$\frac{d\alpha}{dt} = A\exp\left(-\frac{E_a}{RT}\right) f(\alpha) h\left(p(CO_2), P_{eq}(T)\right), \quad (3)$$

where $P_{eq}(T)$ is the equilibrium pressure of the reaction. Various forms of AF have been proposed and examined for describing the kinetics of the thermal decomposition of inorganic solids under different partial pressures of evolved gas, including the most commonly used form:[21, 23-25, 41-43]

$$h\left(p(CO_2), P_{eq}(T)\right) = 1 - \frac{p(CO_2)}{P_{eq}(T)} \quad (4)$$

However, it has been suggested that conventionally applied AFs do not always satisfy the universal kinetic description for the thermal decomposition of carbonates under different heating and $p(CO_2)$ conditions showing different Arrhenius-type plots for the reactions at individual $p(CO_2)$ values.[25] Furthermore, the thermal decomposition of inorganic solids is generally described by the physicogeometrical consecutive process of surface reaction and subsequent internal reaction in each sample particle.[34-36, 44-46] Thus, the effect of the atmospheric $p(CO_2)$ on the kinetics might be different for individual physico-geometrical reaction steps that occur on the surface and at the reaction interface within the sample particles. Recently, we achieved a universal kinetic description of the thermal dehydration and dehydroxylation of inorganic salts over different temperatures and atmospheric water vapor pressure ($p(H_2O)$) values,[47-50] by introducing an analytical form of AF into the kinetic equation. The same was succeeded for the thermal decomposition of $ZnCO_3$ over different temperatures and $p(CO_2)$ values.[51] Furthermore, the universal kinetic description was applied to each reaction step in physico-geometrical consecutive processes of thermal dehydration and decomposition, enabling to characterize the effect of $p(H2O)$ or $p(CO_2)$ on each reaction step and to track its changes as the reaction step progressed.[47-51] The effect of $p(CO_2)$ on the overall kinetics of the thermal decomposition of $CaCO_3$ in perlite concrete and Portland cement could also be described universally over different temperatures and $p(CO_2)$ values.[52-53] However, the effect of $p(CO_2)$ on the kinetics of the thermal decomposition of $CaCO_3$ reagent is more significant than the previously studied processes, even when compared with the thermal decomposition of $CaCO_3$ in cement and concrete materials, which is expected from the significant shift of the thermoanalytical curves along with the temperature coordinate as the $p(CO_2)$ value increases (Figure 1). Therefore, achieving the universal kinetic description for the thermal decomposition of $CaCO_3$ is a necessary step toward the theoretical reformation of the kinetics of the thermal decomposition of solids as functions of temperature, conversion, and partial pressure of product gas. Furthermore, deducing from the significant effect of atmospheric $p(CO_2)$, the self-generated CO_2 by the reaction as the gaseous product should also be considered for elucidating the kinetic features across different temperatures and $p(CO_2)$ values. In this article, the universal kinetic descriptions of the thermal decomposition of $CaCO_3$ in terms of overall reaction and physico-geometrical consecutive process through parameterizing the effect of $p(CO_2)$ are demonstrated to provide further insight into the well-established understanding of the thermal

decomposition process. Moreover, the possibility to estimate the contribution of the self-generated CO_2 to the kinetics is examined on the basis of the established universal kinetic description of the thermal decomposition of $CaCO_3$.

2. Experimental Section

2.1 Sample descriptions

Commercially available $CaCO_3$ reagent (>99.9%; Wako Pure Chem.) was used as the sample without any further purification and sieving. The sample was characterized using powder X-ray diffraction measurement (RINT-2200V, Rigaku) to have calcite structure ($CaCO_3$, trigonal, S.G. = *R*- 3*c*(167), $a = b = 4.9896$, $c = 17.0610$, $\alpha = \beta = 90.000$, $\gamma = 120.000$, ICDD PDF 00-047-1743)54 (Figure S1). The morphology of the sample particles was investigated by microscopic observations using scanning electron microscopy (SEM, JSM-6510, JEOL) after coated with a thin platinum layer by sputtering. The calcite sample was confirmed as agglomerates of sub-micrometer sized cubic shaped particles (Figure S2). The specific surface area of the calcite sample was determined to be 6.56 ± 0.01 m^2 g^{-1} by the Brunauer–Emmett–Teller (BET) single-point method55 using an instrument (FlowSorb II, micromeritics).

2.2 Kinetic data measurements.

The thermal decomposition process of the $CaCO_3$ sample was investigated using a TG–DTA instrument (TG-8121, Thermoplus Evo2 system, Rigaku). An approximately 2.5 mg sample (sample mass (m_0)) was weighed in a platinum pan (diameter: 5 mm; height: 2.5 mm). The TG–DTA measurements were performed using different heating program modes such as isothermal, linear nonisothermal, and constant transformation rate thermal analysis (CRTA) [56-57] modes in a stream of dry N_2 gas ($p(H_2O) < 0.2$ kPa), dry air ($p(H_2O) < 0.2$ kPa; $p(CO_2) = \sim 5 \times 10^{-2}$ kPa), or N_2–CO_2 mixed gases characterized by different $p(CO_2)$ ($p(H_2O) < 0.2$ kPa) at a flow rate (q_v) of 300 cm^3 min^{-1}. All gases supplied from the respective bombs were passed through drying tubes containing a molecular sieve (SA, GL Science). After passing the drying tube, the $p(H_2O)$ value of each gas was confirmed to be lower than 0.2 kPa using a hygrometer (HUHBN-HT20E, NGK Spark Plug). For the measurements in a stream of N_2–CO_2 mixed gas, the $p(CO_2)$ value was regulated by controlling the flow rates of dry N_2 and CO_2 gases to be mixed in a gas mixing tube before being introducing into the TG–DTA instrument by monitoring the CO_2 concentration of the outlet gas from the instrument using CO_2 meters (LX-720 for low concentration (0–5000 ppm) and LX-710 for high concentration (0–20%), IIJIMA). Initially, the effect of $p(CO_2)$ on the thermal decomposition of the $CaCO_3$ sample was investigated by recording TG–DTA curves under linear nonisothermal heating mode at a β of 5 K min^{-1} under different atmospheric $p(CO_2)$ conditions (Figure 1). After that, systematic TG–DTA measurements were performed under different heating program modes by selecting five $p(CO_2)$ values of 0, 1, 5, 10, and 20 kPa. Under isothermal heating mode, the sample was heated from room temperature to a programmed temperature at a β of 10 K min^{-1} and the temperature was maintained during the mass-loss measurements for the thermal decomposition. The temperature ranges of the isothermal temperature programs were 798–833 K, 981–944 K, 1013–1038 K, 1046–1068 K, and 1084–1104 K for measurements at $p(CO_2)$ values of 0, 1, 5, 10, and 20 kPa, respectively. The measurements under linear nonisothermal conditions were performed by

heating the sample from room temperature to 1173 K at different β values of 0.5, 1, 2, 3, 5, 7, and 10 K min^{-1} under respective $p(CO_2)$ conditions. In the CRTA mode, the sample was heated from room temperature to 1173 K at a β of 2 K min^{-1}, while during the mass-loss process, the mass-loss rate was regulated to be different constant rates (C) at 2.5, 5.0. 7.5, 10.0, 12.5, and 15.0 μg min^{-1} through feedback control of the sample temperature by monitoring the mass-loss rate.

3. Results and Discussion

3.1 Kinetics of the thermal decomposition in a stream of dry N_2 gas

The reported kinetic results for the thermal decomposition of $CaCO_3$ in an inert gas atmosphere vary widely depending on the sample, measurement conditions, and kinetic calculation method employed.[37] Therefore, the kinetics of the reaction in a stream of dry N_2 gas was reexamined to show the applicability of the conventional kinetic analysis based on eq. (2) and provide the basis for the advanced kinetic approach considering the effect of CO_2 on the reaction kinetics based on eq. (3). After the TG–DTG measurements under different m_0 and flow rate of dry N_2 gas conditions were examined, measurement conditions of m_0 = 2.50 ± 0.05 mg and q_v = 300 cm^3 min^{-1} were selected as suitable for collecting the kinetic data.[58] TG–DTG measurements were performed using isothermal (798 ≤ T/K ≤ 834), linear nonisothermal (0.5 ≤ β/K min^{-1} ≤ 10), and CRTA (2.5 ≤ C/μg min^{-1} ≤ 15) modes under the selected conditions (Figure S3). The TG–DTG curves were converted to the kinetic data comprising a series of numerical data (time, T, α, dα/dt) by calculating the α value as the ratio of the mass-loss value at a time with reference to the total mass-loss value at the end of the reaction. The logarithmic form of eq. (2) was used for the kinetic calculation assuming an ideal single-step reaction described by two variables of α and T.

$$\ln\left(\frac{\mathrm{d}\alpha}{\mathrm{d}t}\right) = \ln[Af(\alpha)] - \frac{E_\mathrm{a}}{RT} \qquad (5)$$

From eq. (5), the kinetic relationships are represented in the 3D coordinates of T^{-1}, α, and ln(dα/dt). The kinetic data recorded under different heating modes systematically covered a curved surface in the 3D kinetic coordinate (Figure S4). Figure 2 shows the results of the conventional kinetic analysis for the thermal decomposition of $CaCO_3$ in a stream of dry N_2 gas. The isoconversional kinetic relationship occurs in the 2D plane of ln(dα/dt) versus T^{-1}, perpendicular to α. The graphs of ln(dα/dt) versus T^{-1} at a selected α value (Friedman plot[59]) exhibited statistically significant linear correlations, including all data points that originated from the kinetic data under different heating modes (Figure 2(a)). The slope of the Friedman plot was practically invariant irrespective of α value. Therefore, the constant Ea value was obtained during the reaction except the very beginning and ending of the reaction (Figure 2(b)), which was characterized by the average E_a value of 186.5 ± 0.6 kJ mol^{-1} in 0.1 ≤ α ≤ 0.9. The revealed isoconversional kinetic relationship approximately satisfies the single-step assumption showing a constant E_a during the reaction. For such a kinetic process, the isothermal kinetic relationship appears in the 2D plane of ln(dα/dt) versus α perpendicular to T^{-1}. One of such an isothermal plane appears at an infinite temperature ($T^{-1} \rightarrow 0$). The isothermal relationship at infinite temperature is reproduced by an experimental master plot of (dα/dθ) versus α:[60-65]

$$\frac{\mathrm{d}\alpha}{\mathrm{d}\theta} = \left(\frac{\mathrm{d}\alpha}{\mathrm{d}t}\right)\exp\left(\frac{E_\mathrm{a}}{RT}\right) = Af(\alpha), \tag{6}$$

with $$\theta = \int_0^t \exp\left(-\frac{E_\mathrm{a}}{RT}\right)\mathrm{d}t,$$

where θ denotes hypothetical reaction time at infinite temperature (Ozawa's generalized time[66-67]). The experimental master plot for the thermal decomposition of $CaCO_3$ in a stream of dry N_2 gas was characterized by the deceleration rate behavior as the reaction proceeded after a short acceleration period at the beginning of the reaction (Figure 2(c)). According to eq. (6), the A value was determined by fitting the experimental master plot using appropriate $f(\alpha)$. For the overall process ($0.01 \leq \alpha \leq 0.99$), an empirical kinetic model known as the Šesták–Berggren model with three kinetic exponents (SB(m, n, p))[68-70] was used to fit the experimental master plot characterized by the maximum rate at $\alpha = 0.19$.

$$\mathrm{SB}(m,n,p): f(\alpha) = \alpha^m(1-\alpha)^n[-\ln(1-\alpha)]^p \tag{7}$$

Since the acceleration period is limited ($\alpha \leq 0.19$) and the subsequent process is characterized by deceleration with a convex shape, the experimental master plot in $0.30 \leq \alpha \leq 0.90$ was also fitted using the phase boundary-controlled model (R(n)).

$$\mathrm{R}(n): f(\alpha) = n(1-\alpha)^{1-1/n}, \tag{8}$$

where n originally referred to the dimension of the interface shrinkage. In both fitting examinations using SB(m, n, p) and R(n), the statically significant fit was obtained with the determination coefficient of the nonlinear least-squares analysis (R2) better than 0.99. The kinetic exponents in SB(m, n, p) or R(n) and the corresponding A values determined through the model fitting are listed in Table 1. The formal kinetic analysis results indicate a consecutive physico-geometrical process comprising the surface reaction and the subsequent phase boundary-controlled reaction characterized by the acceleration and deceleration periods, respectively. Although a more detailed kinetic analysis may be possible, the overall kinetic behavior of the thermal decomposition of $CaCO_3$ in an inert gas atmosphere can be formally described by the conventional kinetic approach without considering the effect of CO_2 when the kinetic data were measured with due attention to reducing unavoidable influences of mass and heat transfer phenomena.

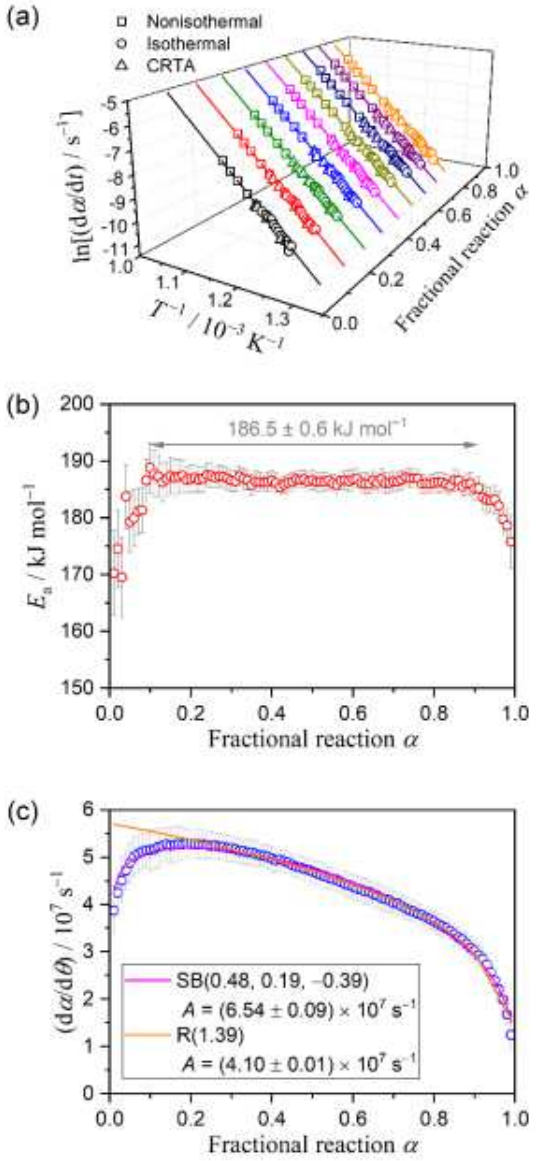

Figure 2. Formal kinetic analysis of the thermal decomposition of $CaCO_3$ in a stream of dry N_2 gas: (a) Friedman plots at different α values, (b) E_a values at different α, and (c) experimental master plot of $(d\alpha/d\theta)$ versus α and fit curves using SB(m, n, p) and R(n) functions.

Table 1. A values and kinetic exponents for the thermal decomposition of $CaCO_3$ in a stream of dry N_2 gas, determined by fitting the experimental mater plot using different $f(\alpha)$

$f(\alpha)$	A / s^{-1}	m	n	p	$R^{2,a}$
SB(m, n, p) [b]	$(6.54 \pm 0.09) \times 10^7$	0.48 ± 0.11	0.19 ± 0.04	-0.39 ± 0.11	0.9933
R(n) [c]	$(4.10 \pm 0.01) \times 10^7$	-----	1.39 ± 0.01	-----	0.9980

[a] Determination coefficient of the nonlinear least-squares analysis.

[b] $0.01 \leq \alpha \leq 0.99$.

[c] $0.30 \leq \alpha \leq 0.90$.

3.2 Kinetics of the induction period at different $p(CO_2)$ values

Figure 3 shows the TG–DTG curves for the thermal decomposition of $CaCO_3$ under isothermal conditions at various temperatures in a stream of N_2–CO_2 mixed gas characterized by different $p(CO_2)$ values, i.e., 1, 5, 10, and 20 kPa. The induction period (IP) was observed irrespective of $p(CO_2)$ value, which was not detected for the reaction in a stream of dry N_2 gas. Sigmoidal shape of the subsequent mass-loss curves was a specific feature. The reaction temperatures suitable for measuring the entire mass loss process under isothermal conditions were systematically shifted to higher temperature regions by increasing the $p(CO_2)$ value.

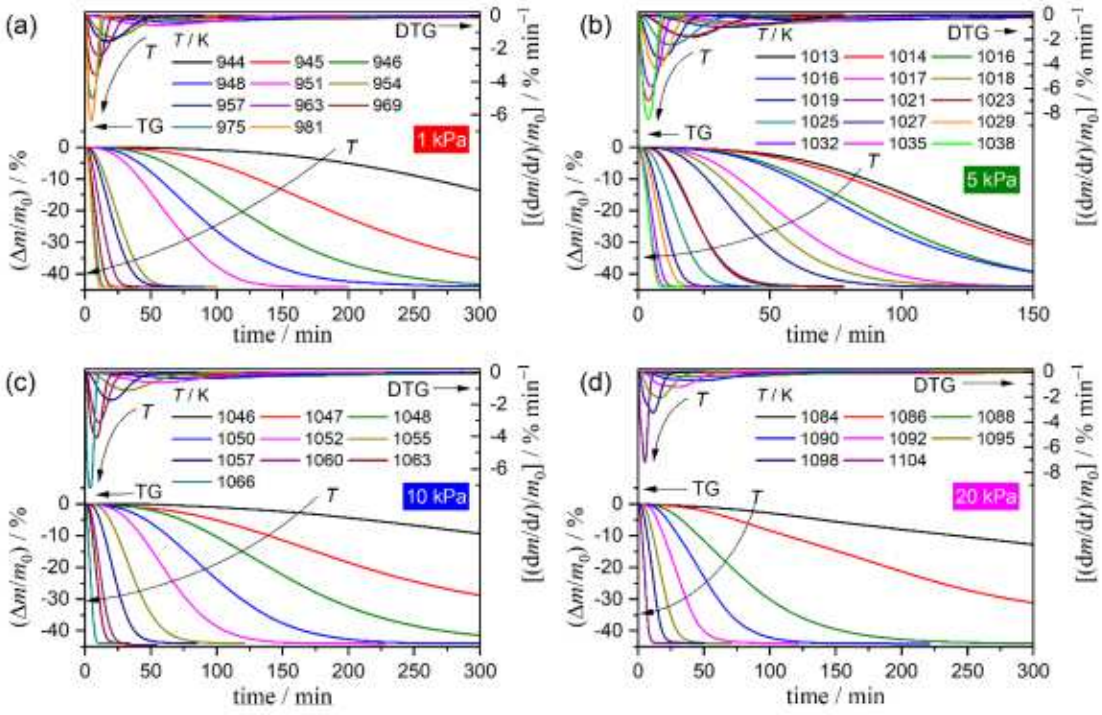

Figure 3. TG–DTG curves under isothermal heating mode for the thermal decomposition of $CaCO_3$ in a stream of N_2–CO_2 mixed gas characterized by different $p(CO_2)$ values (q_v = 300 cm^3 min^{-1}): (a) 0.99±0.03 kPa (m_0 = 2.479±0.061 mg), (b) 5.00±0.01 kPa (m_0 = 2.517±0.066 mg), (c) 10.01±0.02 kPa (m_0 = 2.461±0.140 mg), and (d) 20.03±0.04 kPa (m_0 = 2.524±0.039 mg). Time zero was defined as the time at which the temperature reached to the programmed temperature.

The IP duration (t_{IP}) was empirically determined from the TG–DTG curves by reading the time interval from when the sample temperature reached the programmed temperature to the extrapolated onset time of the DTG peak. Figure 4 shows the conventional kinetic analysis for the IP without considering the effect of $p(CO_2)$. In each $p(CO_2)$ value, t_{IP} value increased exponentially with decreasing the temperature (Figure 4(a)). The temperature range in which the IP was recorded was systematically shifted to higher temperatures with an increase in the $p(CO_2)$ value. Since the reciprocal value of t_{IP} can be the average rate of IP, the temperature dependence of t_{IP}^{-1} at each $p(CO_2)$ value was examined using the conventional kinetic equation based on the Arrhenius equation: [46, 71-75]

$$\frac{1}{t_{IP}} = A_{IP}\exp\left(-\frac{E_{a,IP}}{RT}\right) f(\alpha_{IP}), \qquad (9)$$

where A_{IP} and $E_{a,IP}$ are the preexponential factor and activation energy for the IP, respectively. The conversion of IP is empirically expressed by α_{IP}, and the function $f(\alpha_{IP})$ expresses the change in the reaction rate as the IP process proceeds. The $\ln(1/t_{IP})$ versus T^{-1} plots at each $p(CO_2)$ value exhibited a statistically significant linear correlation (Figure 4(b)). However, approximate trend of the increase in the slope with an increase in the $p(CO_2)$ value was observed. The $E_{a,IP}$ and A_{IP} values determined from the Arrhenius plot without considering the effect of $p(CO_2)$ value are listed in Table S1. Both $E_{a,IP}$ and A_{IP} values exhibited significantly large values that cannot be acceptable because of physico-chemical considerations based on eq. (9) and increased dramatically with increasing $p(CO_2)$ value, i.e., ($E_{a,IP}$/kJ mol^{-1}, $\ln[A_{IP} \cdot f(\alpha_{IP})/s^{-1}]$) = (1826, 225) at $p(CO_2)$ = 1 kPa and (3253, 353) at $p(CO_2)$ = 20 kPa.

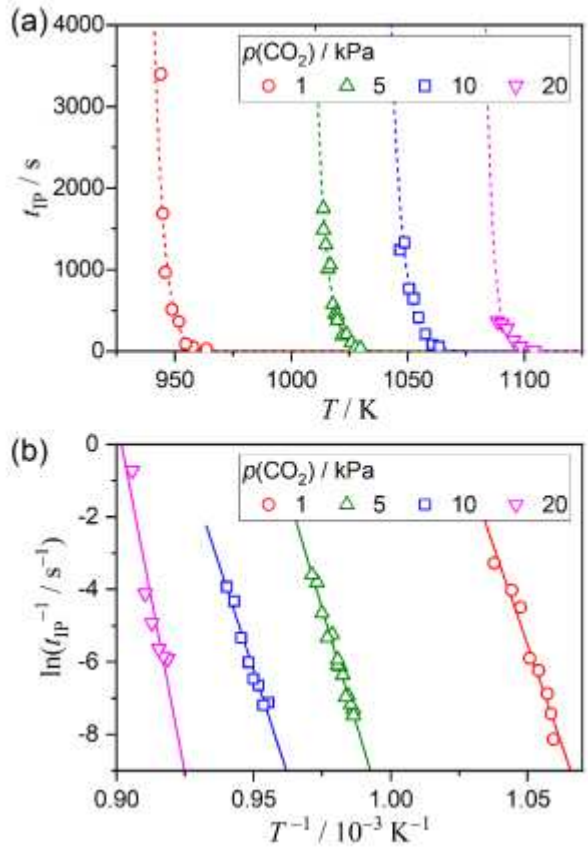

Figure 4. Conventional kinetic analysis for IP without considering the effect of $p(CO_2)$: (a) duration of IP at different temperatures at each $p(CO_2)$ value and (b) Arrhenius plots for IP at each $p(CO_2)$ value. The broken lines in (a) were calculated using the kinetic parameters determined in (b).

The unexpectedly large Arrhenius parameters determined for the IP at each $p(CO_2)$ value and their variations with the $p(CO_2)$ value indicate that the $p(CO_2)$ should be considered in the kinetic description. The $p(CO_2)$ terms can be introduced into the kinetic equation for the IP process as an AF.[47-51]

$$\frac{1}{t_{IP}} = A_{IP}\exp\left(-\frac{E_{a,IP}}{RT}\right) f(\alpha_{IP}) h\left(p(CO_2), P_{eq}(T)\right) \qquad (10)$$

However, no distinguishable improvement of the Arrhenius plots could be observed when the conventional AF (eq. (4)) was introduced into eq. (10). Therefore, possible forms of the AF for the IP of the thermal decomposition of $CaCO_3$ was explored by considering the consecutive elementary steps of the surface nucleation based on the classical nucleation theory, which is composed of (1) creation of the interstitial CO_2 defect in the $CaCO_3$ crystal surface, (2) consumption of the interstitial CO_2 defect, (3) desorption of CO_2 molecule, and (4) consumption of the defects and formation of the O element in CaO crystal. Then, one of the elementary steps was considered the rate-limiting step (rate-limiting step approximation), and the other elementary steps were assumed to be at equilibrium (steady-state approximation). Table 2 summarizes elementary steps of surface nucleation (Kröger's notation[76]), the equilibrium constant of each elementary step, and kinetic equations derived by selecting an elementary step

as the rate-limiting step. The equilibrium constant (K) for the overall IP process is expressed by:

$$K = K_1 K_2 K_3 K_4^{1/n} = \exp\left(-\frac{\Delta_r G^\circ}{RT}\right) = P_{eq}(T), \quad (11)$$

where K_1–K_4 are the equilibrium constants for the elementary processes (1)–(4), respectively. ΔrG° is the standard Gibbs energy of the thermal decomposition of $CaCO_3$. $P_{eq}(T)$ (atm) is the equilibrium pressure of the reaction in eq. (1) at a T. Therefore, all the kinetic equations listed in Table 2 are composed of $p(CO_2)$ and $P_{eq}(T)$. Figure S5 shows the temperature dependence of $P_{eq}(T)$ for the thermal decomposition of $CaCO_3$, which was calculated based on eq. (11) using a thermodynamic database (MALT2, Kagaku Gijutsu-Sha).[77-78] With reference to the $P_{eq}(T)$ versus T curve, the observed IP process proceeds at a higher temperature than the equilibrium temperature at each controlled $p(CO_2)$ value and a lower $p(CO_2)$ value than the $P_{eq}(T)$ value at the respective measured temperatures.

Table 2. Elementary steps of the surface nucleation for the thermal decomposition of $CaCO_3$, equilibrium constants (K_i) for each elementary step, and the kinetic equations derived based on the assumptions that the overall process is regulated by the selected elementary step (rate-limiting step approximation) and the other elementary steps are at equilibrium (steady-state approximation)

i	elementary step	equilibrium constant, K_i	reaction rate, v_i
1	$\mathrm{CO_{3}}_{\mathrm{CO_3}} \rightleftharpoons \mathrm{CO_{2}}_{i} + \mathrm{O}_{\mathrm{CO_3}}$	$K_1 = [\mathrm{CO_{2}}_{i}][\mathrm{O}_{\mathrm{CO_3}}]$	$v_1 = k_1\left(1 - \frac{p(\mathrm{CO_2})}{P_{\mathrm{eq}}(T)}\right)$
2	$\mathrm{CO_{2}}_{i} + (\mathrm{S}) \rightleftharpoons \mathrm{CO_2} - (\mathrm{S})$	$K_2 = \frac{[\mathrm{CO_2} - (\mathrm{S})]}{[\mathrm{CO_{2}}_{i}][(\mathrm{S})]}$	$v_2 = k_2 \frac{K_1 K_3 {K_4}^{1/n}}{K_3 + p(\mathrm{CO_2})}\left(1 - \frac{p(\mathrm{CO_2})}{P_{\mathrm{eq}}(T)}\right)$
3	$\mathrm{CO_2} - (\mathrm{S}) \rightleftharpoons \mathrm{CO_2(g)} + (\mathrm{S})$	$K_3 = \frac{p(\mathrm{CO_2})[(\mathrm{S})]}{[\mathrm{CO_2} - (\mathrm{S})]}$	$v_3 = k_3 \frac{K_1 K_2 {K_4}^{1/n}}{1 + K_1 K_2 {K_4}^{1/n}}\left(1 - \frac{p(\mathrm{CO_2})}{P_{\mathrm{eq}}(T)}\right)$
4	$n\mathrm{O}_{\mathrm{CO_3}} \rightleftharpoons n\mathrm{O_O}$	$K_4 = \frac{[\mathrm{O_O}]^n}{[\mathrm{O}_{\mathrm{CO_3}}]^n}$	$v_4 = k_4\left(\frac{K_1 K_2 K_3}{p(\mathrm{CO_2})}\right)^n\left[1 - \left(\frac{p(\mathrm{CO_2})}{P_{\mathrm{eq}}(T)}\right)^n\right]$

Two different forms of the kinetic equation were derived from the considerations based on the rate-limiting step and steady-state approximations.[47-50]

$$v = k'\left(1 - \frac{p(\mathrm{CO_2})}{P_{\mathrm{eq}}(T)}\right) \tag{12}$$

$$v = k''\left(\frac{1}{p(\mathrm{CO_2})}\right)^{n}\left[1 - \left(\frac{p(\mathrm{CO_2})}{P_{\mathrm{eq}}(T)}\right)^{n}\right] \tag{13}$$

where k' and k'' are the apparent rate constant at a T. Notably, all pressure terms in eqs. (12) and (13) are expressed with the unit in atm. Thereafter, an analytical form of the AF, $h(p(\mathrm{CO_2}), P_{\mathrm{eq}}(T))$, with variable exponents a and b were derived by combining eqs. (12) and (13).[47-50]

$$h\left(p(\mathrm{CO_2}), P_{\mathrm{eq}}(T)\right) = \left(\frac{1}{p(\mathrm{CO_2})}\right)^{a}\left[1 - \left(\frac{p(\mathrm{CO_2})}{P_{\mathrm{eq}}(T)}\right)^{b}\right] \tag{14}$$

where all pressure terms are in the unit of atm. Considering the role of the atmospheric CO_2, the first factor of the AF, i.e., $p(\mathrm{CO_2})^{-a}$, is also the necessary term to express the retardation effect depending on the $p(\mathrm{CO_2})$ value. Therefore, different values of a and b were allowed as the formal kinetic expression in this study. The Arrhenius plot for the IP based on eq. (10) accompanied by the AF in eq. (14), i.e., the plot of ln $[t_{\mathrm{IP}} \cdot h(p(\mathrm{CO_2}), P_{\mathrm{eq}}(T))]^{-1}$ versus T^{-1}, was examined, during which the exponents (a, b) in eq. (14) were optimized to provide the best linear correlation of the Arrhenius plot. Figure 5 shows the extended Arrhenius plots considering $p(\mathrm{CO_2})$ as a parameter to determine the reaction rate. With the optimized exponents (a, b) = (10.3, 31.5), the Arrhenius plots exhibited the statistically significant linear correlation (correlation coefficient γ = -0.9996) over all data points recorded at different temperatures and $p(\mathrm{CO_2})$ values. From the extended Arrhenius plot, the Arrhenius parameters ($E_{\mathrm{a,IP}}$/kJ mol^{-1}, ln $[A_{\mathrm{IP}} \cdot f(\alpha_{\mathrm{IP}})/\mathrm{s}^{-1}]$) were determined to be (1893 ± 10, 186 ± 1). Therefore, using the optimized kinetic exponents (a, b) and the apparent Arrhenius parameters, the kinetic behavior of the IP at different temperatures and $p(\mathrm{CO_2})$ values can be universally described. The linear correlation over all data points at different $p(\mathrm{CO_2})$ values could not be achieved when the first part of the AF, i.e., $p(\mathrm{CO_2})^{-a}$, was canceled by setting a = 0. However, the large value of b = 31.5 cannot have any physical significance. A comparable linear correlation with γ = -0.9995 was obtained when the Arrhenius plot was reexamined by fixing b = 1 (Figure 5). With (a, b) = (9.50, 1), the Arrhenius plot provided the Arrhenius parameters ($E_{\mathrm{a,IP}}$/kJ mol^{-1}, ln $[A_{\mathrm{IP}} \cdot f(\alpha_{\mathrm{IP}})/\mathrm{s}^{-1}]$) = (1752 ± 10, 173 ± 1). The unexpectedly large $E_{\mathrm{a,IP}}$ value should be interpreted by considering the rate-limiting step and steadystate approximations used for modeling the universal kinetic description over different $p(\mathrm{CO_2})$ values. Namely, the Arrhenius-type plots in Figure 5 reflect both the temperature dependence of the average reaction rate of the IP (t_{IP}^{-1}) and $P_{\mathrm{eq}}(T)$ via a complex combination of the phenomena expressed by eqs. (10) and (11). The optimized a value was significantly larger than the previously reported a values for the IP processes of the thermal dehydration and dehydroxylation of inorganic hydrates and hydroxides over different $p(\mathrm{H_2O})$ values.[47-49] The larger a value indicates a more significant retardation effect on the IP process. An empirical trend has been observed that the larger the a value results in the larger increase in the $E_{\mathrm{a,IP}}$ value from that in a stream of dry N_2 gas comparing the four reported cases of the universal kinetic description for the IP process including the present result.

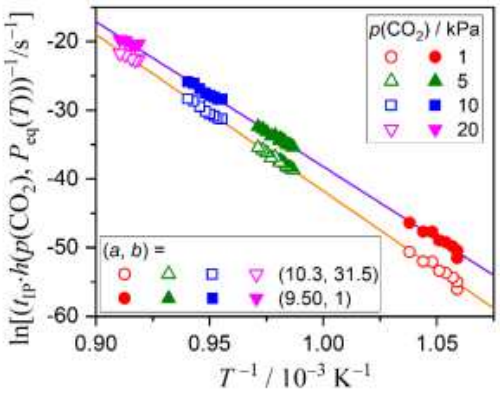

Figure 5. The extended Arrhenius plots based on eqs. (10) and (14) for the IP of the thermal decomposition of $CaCO_3$ over different temperatures and $p(CO_2)$ values.

3.3 Kinetics of the mass-loss process at different $p(CO_2)$ values

In addition to the mass-loss curves recorded under isothermal conditions at different $p(CO_2)$ values shown in Figure 3, those recorded under linear nonisothermal and CRTA conditions were used for the kinetic calculation for the mass-loss process. These mass-loss curves are shown in Figures 6 and 7, respectively. In both heating program modes, a systematic shift of the reaction temperature to higher temperatures was observed with increasing $p(CO_2)$ value, in addition to the systematic shift of the reaction temperature with increasing β and C values at each $p(CO_2)$ value.

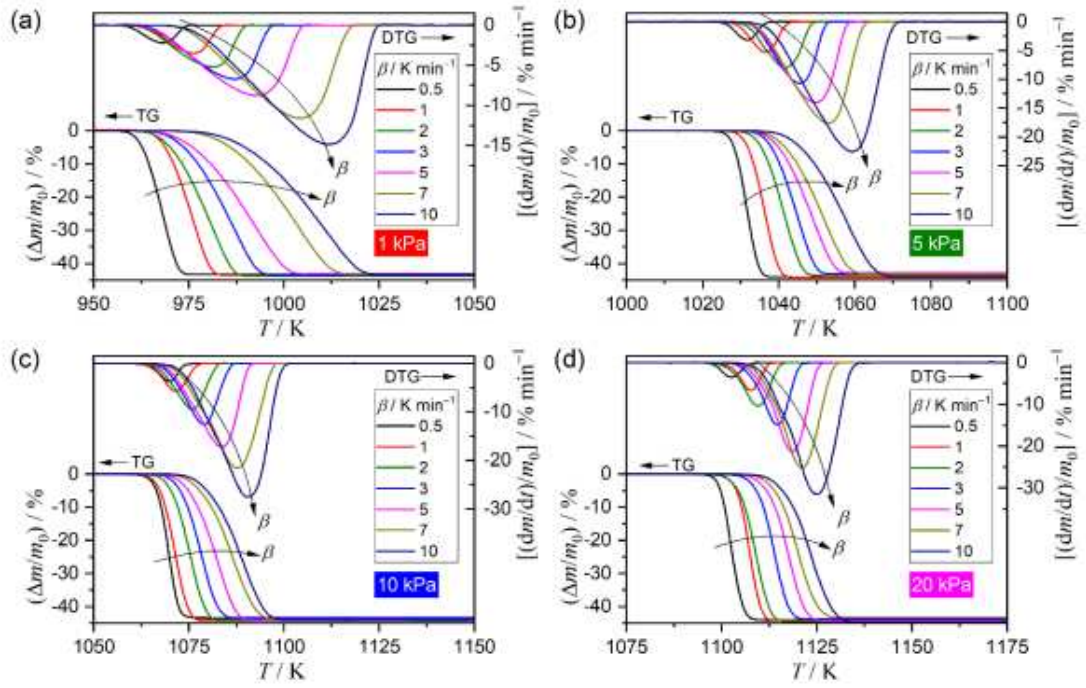

Figure 6. TG–DTG curves for the thermal decomposition of $CaCO_3$ under linear nonisothermal heating mode at various β values in a stream of N_2–CO_2 mixed gas characterized by different $p(CO_2)$ values (q_v = 300 cm^3 min^{-1}): (a) 1.03±0.06 kPa (m_0 = 2.5.03±0.061 mg), (b) 5.00±0.02 kPa (m_0 = 2.492±0.022 mg), (c) 10.04±0.15 kPa (m_0 = 2.514±0.037 mg), and (d) 20.08±0.08 kPa (m_0 = 2.515±0.029 mg).

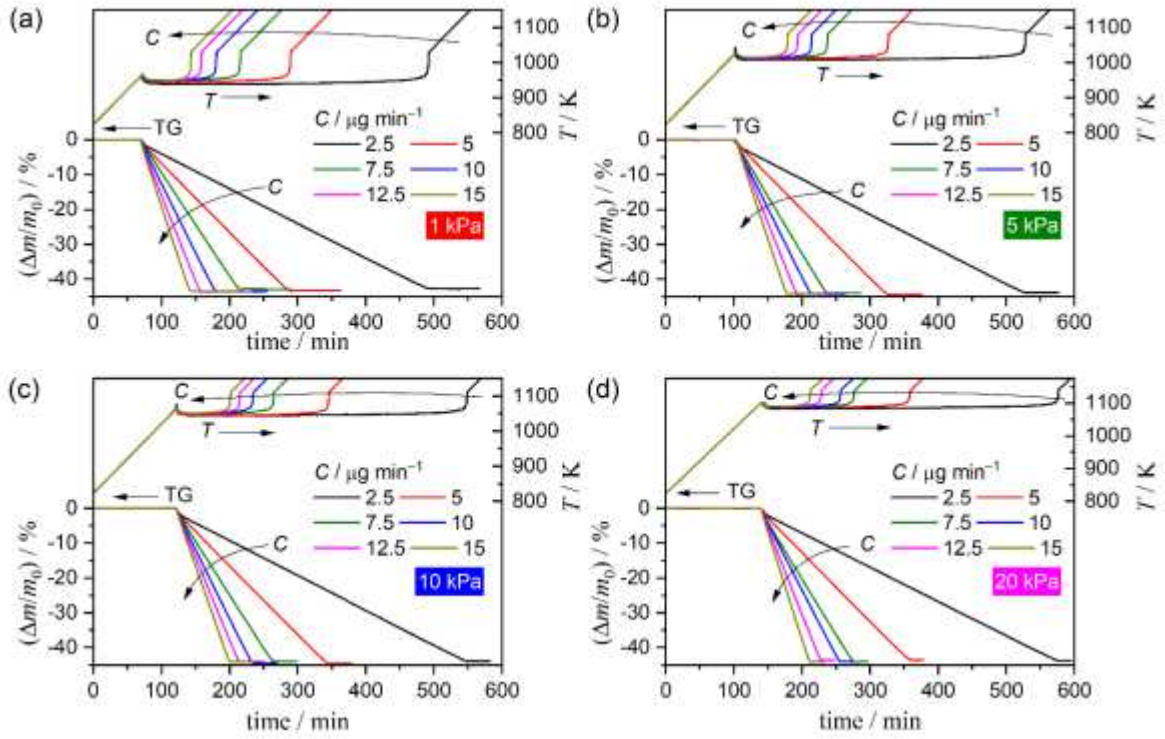

Figure 7. TG–DTG curves for the thermal decomposition of CaCO3 under CRTA heating mode at different *C* values in a stream of N2–CO2 mixed gases characterized by different *p*(CO2) values (*q*v = 300 cm3 min-1): (a) 1.01±0.02 kPa (*m*0 = 2.503±0.025 mg), (b) 5.00±0.01 kPa (*m*0 = 2.464±0.106 mg), (c) 10.01±0.01 kPa (*m*0 = 2.538±0.088 mg), and (d) 20.01±0.05 kPa (*m*0 = 2.486±0.096 mg).

The mass-loss curves for the thermal decomposition of $CaCO_3$ under different heating conditions, including isothermal (Figure 3), linear nonisothermal (Figure 6), and CRTA (Figure 7) modes, were analyzed simultaneously using the formal kinetic analysis procedure via the isoconversional analysis and subsequent master plot method without considering the effect of $p(CO_2)$, as shown in Figure 8. The Friedman plots exhibited approximately linear correlations for the data points at each p(CO2) value, although these were characterized by a convex shape (Figure 8(a)). The slope of the Friedman plot systematically increased with an increase in the $p(CO_2)$ value. These were observed irrespective of α value (Figure S6). The apparent E_a values determined from the slope of the Friedman plot systematically increased with an increase in the $p(CO_2)$ value irrespective of α value (Figure 8(b)). At each $p(CO_2)$ value, the variations in the E_a value were observed in the initial part ($\alpha < 0.3$). The E_a variation was characterized by a systematic decrease at $p(CO_2)$ = 1, 5, and 10 kPa, while at $p(CO_2)$ = 20 kPa by a slight but detectable increase. Note that the E_a values were unexpectedly large compared with those determined for the mass-loss process in a stream of dry N_2 gas (Figure 2(b)). The experimental master plot of $(d\alpha/d\theta)_\alpha/(d\alpha/d\theta)_{0.5}$ versus α for the reaction at each $p(CO_2)$ value was calculated using the average Ea value in the α range of 0.1–0.9 as an approximation by assuming the single-step reaction (Figure 8(c)). Although a slight difference in the shape of the experimental master plot was observed in the first half of the reaction between those at different $p(CO_2)$ values, the experimental master plots were characterized by the maximum reaction rate that appeared midway through the reaction, which was largely different in shape from that in a stream of dry N_2 gas (Figure 2(c)). Table S2 lists the apparent kinetic parameters for the mass-

loss process at each $p(CO_2)$ value obtained from the formal kinetic analysis without considering the effect of $p(CO_2)$.

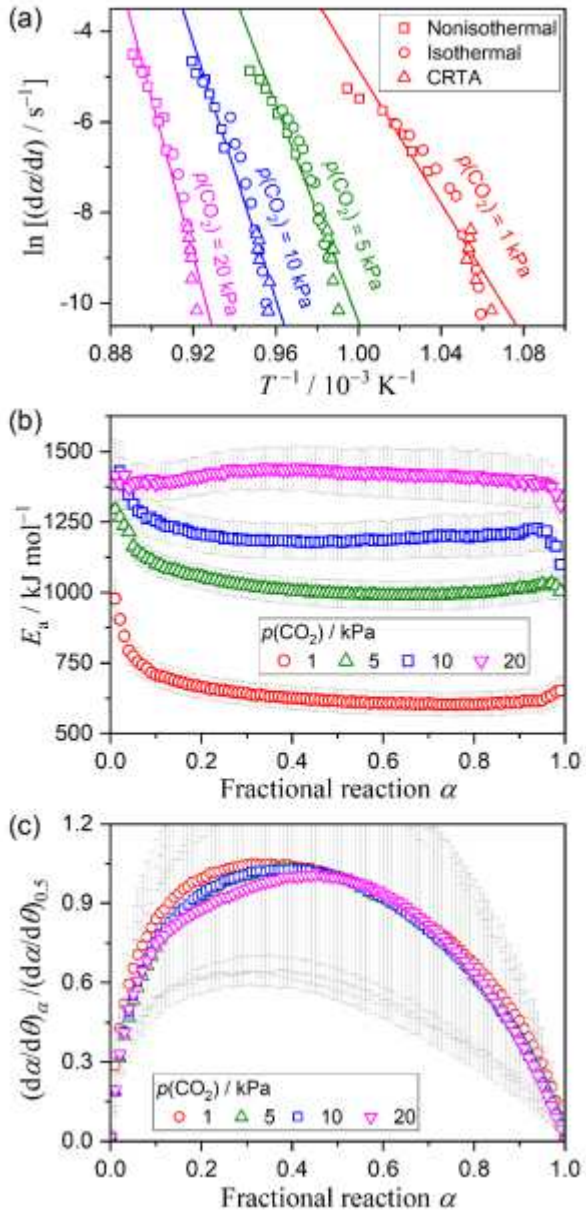

Figure 8. Conventional kinetic analysis for the mass-loss process of the thermal decomposition of $CaCO_3$ at individual $p(CO_2)$ values performed without considering the effect of $p(CO_2)$: (a) Friedman plots at α = 0.5, (b) E_a values at different α, and (c) normalized experimental master plots of $(d\alpha/d\theta)_\alpha/(d\alpha/d\theta)_{0.5}$ versus α.

The necessity of the kinetic approach considering the effect of $p(CO_2)$ on the kinetics of the mass-loss process of the thermal decomposition of $CaCO_3$ is apparent from the results of conventional kinetic analysis for the following reasons: (i) the different isoconversional relationships are observed between the reactions at different $p(CO_2)$ values, (ii) the conventional isoconversional relationship in each reaction at a selected $p(CO_2)$ value is inferior

to the ideal linear correlation, and (iii) the apparent E_a values increase dramatically with an increase in the $p(CO_2)$ value. Thus, an appropriate AF for describing the effect of $p(CO_2)$ on the kinetics of the mass-loss process was explored based on the classical interface reaction theory. For the interfacial process of the thermal decomposition of $CaCO_3$, five consecutive elementary steps were assumed: (1) creation of the interstitial CO_2 defect at the internal interface, (2) diffusion of the interstitial CO_2 defect from the internal to the external interface, (3) consumption of the interstitial defect at the external interface, (4) desorption of CO_2 molecule, and (5) consumption of the defects and formation of the CaO building unit at the internal interface. As in the case of the IP process, one elementary step was selected as the rate-limiting step, and the other elementary steps were assumed to be at equilibrium conditions. The equilibrium constant and the rate of the elementary step derived based on the rate-limiting step and steady-state approximations are listed in Table 3. The two kinetic expressions, which are the same as those presented in eqs. (12) and (13), were obtained. Therefore, the analytical form of AF in eq. (14) was applied to the kinetic analysis of the mass-loss process by introducing it into eq. (3). As aforementioned, the first factor in the AF, i.e., $p(CO_2)^{-a}$, is also needed as a concentration term of the retardant. Therefore, the different values of a and b in the AF were allowed for an empirical approach. The analytical form of AF (eq. (14)) is also the same as those derived for the mass-loss process of the thermal dehydration and decomposition of inorganic salts.[47-51]

Table 3. Elementary steps of the interface reaction of the thermal decomposition of $CaCO_3$, equilibrium constants (K_i) for each elementary step, and the kinetic equations derived based on the assumptions that the overall process is regulated by the selected elementary step (rate-limiting step approximation) and the other elementary steps are at equilibrium (steady-state approximation)

i	elementary step	equilibrium constant, K_i	reaction rate, v_i
1	$\left(\mathrm{CO_{3}}_{\mathrm{CO_3}}\right)_{\mathrm{CaCO_3}} \rightleftarrows \left(\mathrm{O}_{\mathrm{CO_3}}\right)_{\mathrm{CaCO_3}} + \left(\mathrm{CO}_{2,i,\mathrm{int}}\right)_{\mathrm{CaO}}$	$K_1 = [\mathrm{O}_{\mathrm{CO_3}}][\mathrm{CO}_{2,i,\mathrm{int}}]$	$v_1 = k_1\left(1 - \frac{p(\mathrm{CO_2})}{P_{\mathrm{eq}}(T)}\right)$
2	$\mathrm{CO}_{2,i,\mathrm{int}} \rightleftarrows \mathrm{CO}_{2,i,\mathrm{ext}}$	$K_2 = \frac{[\mathrm{CO}_{2,i,\mathrm{ext}}]}{[\mathrm{CO}_{2,i,\mathrm{int}}]} = 1$	$v_2 = \frac{D_{\mathrm{CO}_{2,i}}}{l_0} K_1 K_5\left(1 - \frac{p(\mathrm{CO_2})}{P_{\mathrm{eq}}(T)}\right)$
3	$\mathrm{CO}_{2,i,\mathrm{ext}} + (\mathrm{S}) \rightleftarrows \mathrm{CO_2} - (\mathrm{S})$	$K_3 = \frac{[\mathrm{CO_2} - (\mathrm{S})]}{[(\mathrm{S})][\mathrm{CO}_{2,i,\mathrm{ext}}]}$	$v_3 = k_3 \frac{K_1 K_4 K_5}{K_4 + p(\mathrm{CO_2})}\left(1 - \frac{p(\mathrm{CO_2})}{P_{\mathrm{eq}}(T)}\right)$
4	$\mathrm{CO_2} - (\mathrm{S}) \rightleftarrows \mathrm{CO_2(g)} + (\mathrm{S})$	$K_4 = \frac{p(\mathrm{CO_2})[(\mathrm{S})]}{[\mathrm{CO_2} - (\mathrm{S})]}$	$v_4 = k_4 \frac{K_1 K_3 K_5}{1 + K_1 K_3 K_5}\left(1 - \frac{p(\mathrm{CO_2})}{P_{\mathrm{eq}}(T)}\right)$
5	$n\left(\mathrm{Ca_{Ca}} + \mathrm{O}_{\mathrm{CO_3}}\right)_{\mathrm{CaCO_3}} \rightleftarrows n(\mathrm{Ca_{Ca}} + \mathrm{O_O})_{\mathrm{CaO}}$	$K_5 = \frac{[\mathrm{O_O}]^n}{[\mathrm{O}_{\mathrm{CO_3}}]^n}$	$v_5 = k_5\left(\frac{K_1 K_3 K_4}{p(\mathrm{CO_2})}\right)^n\left[1 - \left(\frac{p(\mathrm{CO_2})}{P_{\mathrm{eq}}(T)}\right)^n\right]$

Taking logarithms of the kinetic equation with the AF considering the effect of $p(CO_2)$ (eq. (3)), the isoconversional plots were examined for the kinetics curves over different $p(CO_2)$ values.[47- 53]

$$\ln \frac{\left(\frac{d\alpha}{dt}\right)}{h\left(p(CO_2), P_{eq}(T)\right)} = \ln[Af(\alpha)] - \frac{E_a}{RT} \qquad (15)$$

Using the AF in eq. (14), the isoconversional kinetic relationship over different temperatures and $p(CO_2)$ values was evaluated at each α value by optimizing the exponents (a, b) in the AF to provide the best linear correlation of the left-hand side of eq. (15) versus reciprocal temperature (extended Friedman plot). Figure 9 shows the results of the kinetic analysis based on eq. (15) accompanied by the AF in eq. (14). At each α value, the extended Friedman plot showed a statistically significant linear correlation over the data points at different temperatures and $p(CO_2)$ values (Figure 9(a)), owing to the optimized exponents (a, b) in the AF (Figure 9(b)). The a and b values rapidly decreased in the initial part of the mass-loss process ($\alpha < 0.1$). i.e., from approximately 7.0 to 5.5 and from 7.8 to 5.8, respectively. During the established part of the mass-loss process, those values gradually decreased to approximately 5.0 and 3.6 at the end, respectively. Notably, the a value maintained constant in the α range of 0.3–0.9 with the average value of 5.11 ± 0.05. The E_a values calculated from the slope of the extended Friedman plot showed an initial decrease from approximately 1350 to 1025 kJ mol^{-1} ($\alpha < 0.3$) and subsequently maintained a constant value to the end of the reaction with average E_a = 1016 ± 5 kJ mol^{-1} ($0.3 \leq \alpha \leq 0.9$). Similar variation trends as the reaction advanced were observed for the a and E_a values, indicating the close correlation. Considering the close correlation observed between exponents (a, b) and E_a value, the isoconversional plots were reexamined using the average (a, b) values in the α range of 0.1–0.9, i.e., (5.17 ± 0.12, 4.39 ± 0.25). No significant deterioration in the linear correlations of the extended Friedman plots was observed when using the average (a, b) values. The E_a value, thus obtained, exhibited relatively small variation as the reaction advanced, characterized by the average E_a of 1023 ± 6 kJ mol^{-1} in $0.1 \leq \alpha \leq 0.9$ (Figure 9(b)). The large apparent E_a value compared with that for the reaction in a stream of dry N_2 gas should be explained by considering the contributions of temperature dependence of the rate constant and $P_{eq}(T)$ into the linear relationship of the extended Friedman plots because of the rate-limiting step and steady-state approximations introduced into the kinetic equation, as in the case for IP process. The rigorous explanation of the apparent E_a value determined by the extended Friedman plot using the intrinsic E_a and enthalpy of the reaction ($\Delta_r H$) is a future challenge. Currently, several discussions on the physical meaning of the apparent E_a value in relation to the intrinsic E_a and $\Delta_r H$ have been reported for the simple case characterized by (a, b) = (0, 1).[40, 79-81] Similar discussions have also been made for the solid–gas reactions with (a, b) = (-1, 0) and (-1, -1).[82-83]

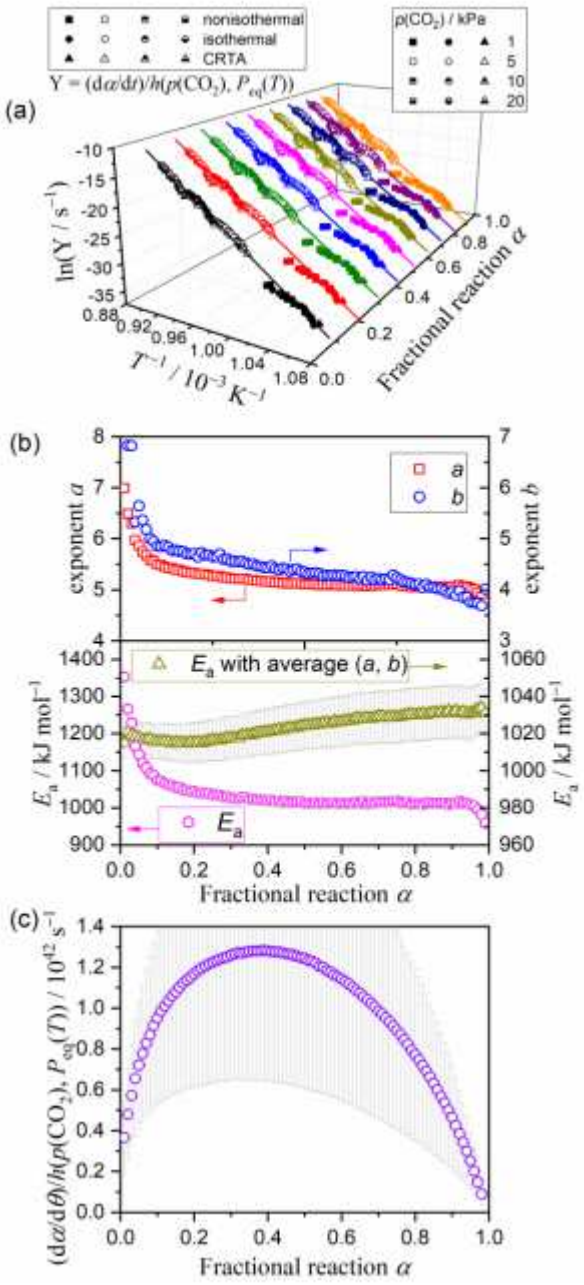

Figure 9. Kinetic results of the isoconversional kinetic analysis considered the effect of $p(CO_2)$ for the thermal decomposition of $CaCO_3$: (a) extended Friedman plots applied to all data points over different temperatures and $p(CO_2)$ values, (b) optimized kinetic exponents (a, b) in the AF and Ea values at different α values, and (c) the extended experimental master plot.

The AF should also be considered in the experimental master plot to describe the kinetic behavior universally over different temperatures and $p(CO_2)$ values.[51, 53]

$$\frac{\left(\frac{d\alpha}{d\theta}\right)}{h\left(p(CO_2), P_{eq}(T)\right)} = \frac{\left(\frac{d\alpha}{dt}\right)}{h\left(p(CO_2), P_{eq}(T)\right)} \exp\left(\frac{E_a}{RT}\right) = Af(\alpha) \qquad (16)$$

Based on the single-step assumption, the average Ea value of 1023 ± 6 kJ mol^{-1} ($0.1 \leq \alpha \leq 0.9$) was used for calculating the extended experimental master plot, with the average (a, b) values ($0.1 \leq \alpha \leq 0.9$). The extended experimental master plot exhibited the maximum rate midway through the reaction at $\alpha = 0.39$ (Figure 9(c)). The rate behavior expected from the experimental master plot is different from a simple contracting geometry model for the thermal decomposition of solids and indicative of the physico-geometrical consecutive process comprised surface reaction (SR) and phase boundarycontrolled reaction (PBR). [44-46]

3.4 Kinetic analysis based on the IP–SR–PBR model at different $p(CO_2)$ values

The appearance of the IP under isothermal conditions irrespective of $p(CO_2)$ values and the rate behavior characterized by a sigmoidal mass-loss curve with the maximum rate midway through the reaction indicate the possible kinetic model as described using the physico-geometrical consecutive process comprising the IP, SR, and PBR. The mathematical formalization of the consecutive IP–SR–PBR process has been achieved by Ogasawara and Koga[46] for the process under isothermal conditions based on Mampel's model.[44] The mathematical modeling for the consecutive SR–PBR process was also achieved by Favergeon et al.[45] For the thermal decomposition of $CaCO_3$ under isothermal conditions at various $p(CO_2)$ values, differential kinetic curves were fitted with the calculated curves based on the kinetic equations for the IP–SR–PBR(n) models with different interface shrinkage dimensions n in the PBR process (Table S3) by optimizing the rate constants for the IP, SR, and PBR(n), i.e., k_{IP}, k_{SR}, and $k_{PBR(n)}$, respectively. For this mathematical procedure, the initial k_{IP} and $k_{PBR(n)}$ values were determined based on the preliminary kinetic analyses for the IP and mass-loss processes summarized in Tables S1 and S2, respectively. The order of the initial k_{SR} value was empirically estimated by graphically comparing the experimental kinetic curve and the calculated curve after the initial k_{IP} and $k_{PBR(n)}$ values were introduced in the kinetic equation. After that, the k_{IP}, k_{SR}, and $k_{PBR(n)}$ values were optimized via nonlinear least-squares analysis based on the Levenberg– Marquardt algorithm. The results of the nonlinear least-squares analysis exhibited the superior fitting of the calculated curve to the experimental kinetic curve when the kinetic equation for the IP–SR–PBR(2) or IP–SR–PBR(3) model was applied irrespective of $p(CO_2)$ value, in which the IP–SR– PBR(2) model indicated a slightly better fitting because of the determination coefficient (R2). Figures 10 and S7 show typical results of the fitting using the IP–SR–PBR(2) and IP–SR–PBR(3) models, respectively. Because the $CaCO_3$ sample was the agglomerate of submicrometer-sized cubic crystal powders (Figure S2), the interface shrinkage dimension between 2 and 3 can be expected as the actual shrinkage dimension in the PBR process.

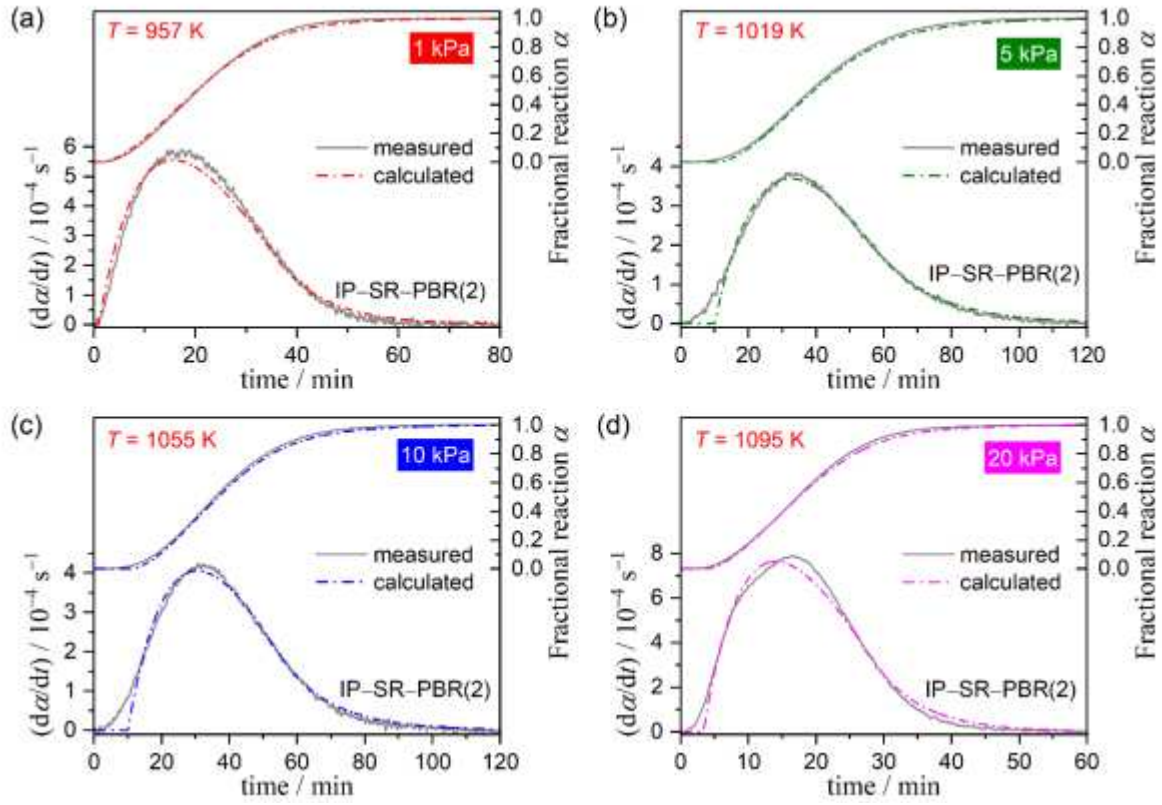

Figure 10. Typical fitting results of the kinetic curves with the IP–SR–PBR(2) model for the thermal decomposition of $CaCO_3$ under isothermal conditions at different $p(CO_2)$ values: (a) 0.96 kPa (T = 957 K), (b) 5.01 kPa (T = 1019 K), (c) 10.02 kPa (T = 1055 K), and (d) 20.04 kPa (T = 1095 K).

Tables S4 and S5 list the optimized k_{IP}, k_{SR}, and $k_{PBR(n)}$ values for each kinetic curve based on the IP–SR–PBR(2) and IP–SR–PBR(3) models, respectively. Preliminarily, the temperature dependence of the rate constants in each physico-geometrical reaction step was examined based on the Arrhenius equation without considering the effect of $p(CO_2)$.

$$k = A\exp\left(-\frac{E_a}{RT}\right) \tag{17}$$

Irrespective of the physico-geometrical reaction step, the conventional Arrhenius plots exhibited the different linear correlations between the reactions at different $p(CO_2)$ values (Figures S8 and S9 for the k_{IP}, k_{SR}, and $k_{PBR(n)}$ values determined based on IP–SR–PBR(2) and IP–SR–PBR(3) models, respectively). The universal description of the temperature and $p(CO_2)$ dependence of the k values in each reactions step was attempted by introducing the AF described in eq. (14) into the Arrhenius equation.

$$k = A\exp\left(-\frac{E_a}{RT}\right)h\left(p(CO_2), P_{eq}(T)\right) \tag{18}$$

Figures 11 and S10 show the extended Arrhenius plots for the k_{IP}, k_{SR}, and $k_{PBR(n)}$ values determined based on the IP–SR–PBR(2) and IP–SR–PBR(3) models, respectively. Through optimizing the exponents (a, b) in eq. (14), the Arrhenius plots of ln [$k/h(p(CO_2), P_{eq}(T))$] versus T^{-1} exhibited the statistically significant linear correlations for the k values over different

temperatures and $p(CO_2)$ values in each reaction step. Table 4 lists the kinetic parameters for each reaction step determined by the extended Arrhenius plots. The kinetic parameters for the IP process coincided with those obtained by the extended Arrhenius plots for the average rate of the IP (Figure 5). The exponents (a, b) for the SR and PBR(n) process corresponded to those values determined through the extended Friedman plot at the initial and established part of the overall reaction, respectively. The E_a and A values decreased as the physico-geometrical reaction step advanced from IP to PBR(n) via SR. The decreasing trend of E_a value as the reaction advanced was also in agreement with that revealed by the extended Friedman plot (Figure 9).

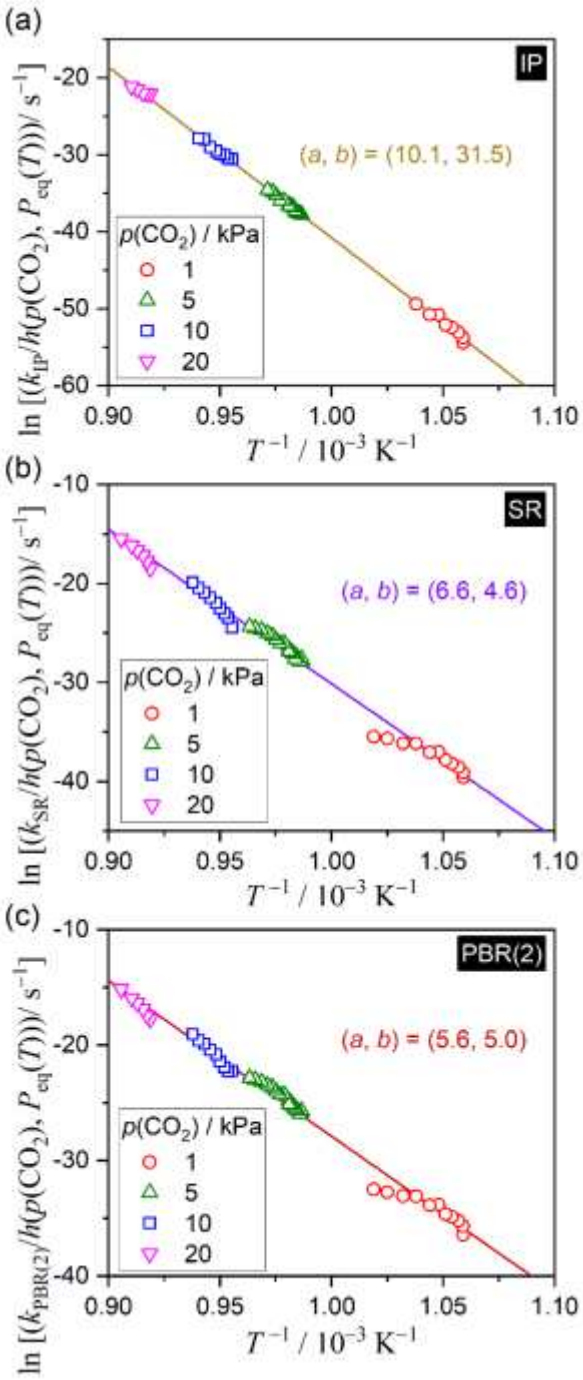

Figure 11. The extended Arrhenius plots for the k_{IP}, k_{SR}, and $k_{PBR(2)}$ values determined based on the IP–SR–PBR(2) model for the respective reaction steps of the thermal decomposition of $CaCO_3$ at different temperatures and $p(CO_2)$ values: (a) IP, (b) SR, and (c) PBR(2).

Table 4. The kinetic parameters for each physico-geometrical reaction step determined by the extended Arrhenius plots of the k values at different temperatures and $p(CO_2)$ values

model	step	a	b	E_a/kJ mol^{-1}	ln[($A/h(p(CO_2), P_{eq}(T))$)/s^{-1}]	$-\gamma$ [a]
IP–SR–PBR(2)	IP	10.1	31.5	1843 ± 9	181 ± 1	0.9996
	SR	6.61	4.61	1297 ± 19	126 ± 3	0.9957
	PBR(2)	5.65	4.96	1122 ± 17	107 ± 2	0.9957
IP–SR–PBR(3)	IP	10.3	31.5	1893 ± 10	186 ± 2	0.9996
	SR	6.34	4.76	1247 ± 19	121 ± 3	0.9955
	PBR(3)	5.79	4.87	1148 ± 17	109 ± 2	0.9957

[a] Correlation coefficient of the linear regression analysis for the extended Arrhenius plot.

3.5 Influences of atmospheric and self-generated $p(CO_2)$

Despite the success of the universal kinetic description for the thermal decomposition of $CaCO_3$ at different temperatures and atmospheric $p(CO_2)$ values, as shown by the kinetic analyses based on the isoconversional relationship (Figure 9) and IP–SR–PBR(n) model (Figure 11), the linear correlation of the universal kinetic plots, i.e., the extended Friedman and Arrhenius plots, was inferior to the ideal linearity as was previously achieved for the thermal dehydration of inorganic hydrate, thermal decomposition of metal hydroxides, and the thermal decomposition of $ZnCO_3$.[47-51] The universal kinetic plot for the IP process was exceptional, giving a superior linear correlation (Figure 11(a)). The difference between the mass-loss process and the IP process is the evolution of CO_2 accompanied by the reaction. Therefore, the contribution of the self-generated CO_2 should be considered for the universal kinetic description for the mass-loss process. The contribution of the self-generated $p(CO_2)$ ($p(CO_2)_{SG}$) can be assumed to be proportional to the evolution rate of CO_2. The effective $p(CO_2)$ ($p(CO_2)_{EF}$) that influences the mass-loss process can be expressed by the weighted sum of the reaction rate and atmospheric $p(CO_2)$ ($p(CO_2)_{ATM}$) with the respective contributions of c and d.

$$p(CO_2)_{EF} = p(CO_2)_{SG} + d \cdot p(CO_2)_{ATM} = c \cdot \left(\frac{d\alpha}{dt}\right) + d \cdot p(CO_2)_{ATM} \quad (19)$$

The extended Friedman plot was reexamined using the $p(CO_2)_{EF}$ instead of atmospheric $p(CO_2)$ by simultaneously optimizing the exponents (a, b) in eq. (14) and the contributions (c, d) in eq. (19). Figure 12 shows the results of the extended Friedman plot modified with the contribution of $p(CO_2)_{SG}$. The linearity of the Friedman plots at all α values was significantly improved (Figure 12(a)). The a value was gradually increased from approximately 9.2 to 11.4 at $\alpha = 0.74$ as the reaction advanced, followed by a decrease at the end of the reaction. Conversely, the b–d values were approximately constant in the major part of the reaction ($0.1 \leq \alpha \leq 0.9$) with the average values of $b = 8.38 \pm 0.73$, $c = 1.19 \pm 0.09$, and $d = 0.31 \pm 0.03$. The possible contribution of the self-generated CO_2 was expected from the constant c value during the reaction. The slightly decreasing trend of d value in the final part of the mass-loss process was indicative of

the limited contribution of the atmospheric CO_2 in the internal reaction of the sample particles. As the reaction progressed, the resulting E_a value increased from approximately 1680 to 2060 kJ mol^{-1}, followed by a decrease at the end of the reaction. Note, the variation trends of a and E_a values were comparable, indicating the necessity to clarify the physico-chemical relationship between a and E_a for interpreting the significance of the unexpectedly large E_a value.

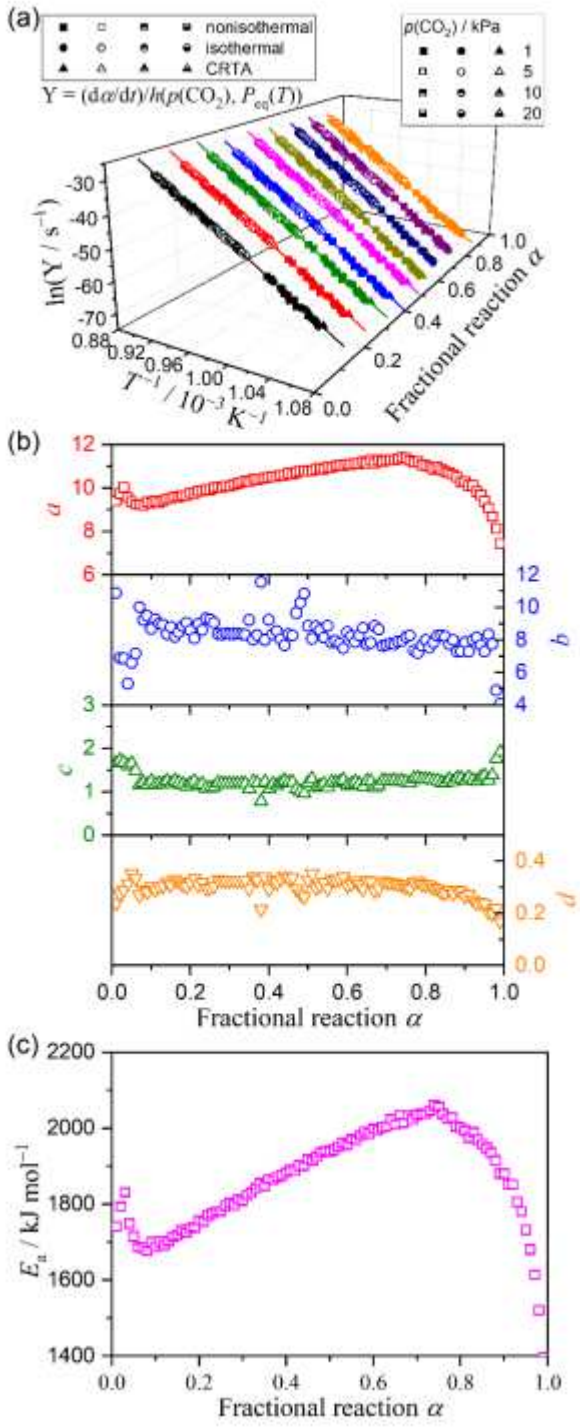

Figure 12. The results of the extended Friedman plots over different temperatures and $p(CO_2)$ values, modified with the contributions of the self-generated CO_2 and atmospheric CO_2 with the coefficients c and d, respectively: (a) modified extended Friedman plots at different α values from 0.1 to 0.9 in steps

of 0.1, (b) the exponents (a, b) in the AF and the coefficients (c, d) at different α values, and (c) E_a values at different α values.

Similarly, for the extended Arrhenius plots for the SR and PBR processes, the $p(CO_2)_{SG}$ is considered approximately proportional to the k_{SR} and $k_{PBR(n)}$ values.

$$p(CO_2)_{EF} = p(CO_2)_{SG} + d \cdot p(CO_2)_{ATM} = c \cdot k + d \cdot p(CO_2)_{ATM} \quad (20)$$

The introduced approximation means the constant contribution of the self-generated $p(CO_2)$ during the reaction. Figures 13 and S11 show the extended Arrhenius plots over different temperatures and $p(CO_2)$ values, modified with the contributions of $p(CO_2)_{SG}$ and $p(CO_2)_{ATM}$ for the k values derived based on IP–SR–PBR(2) and IP–SR–PBR(3) models, respectively. Significant improvements in the linearity of the Arrhenius plots were observed in both the SR and PBR(n) processes. Table 5 lists the kinetic parameters determined by the extended Arrhenius plots modified with the contributions of $p(CO_2)_{SG}$ and $p(CO_2)_{ATM}$. The exponents (a, b) in the AF (eq. (14)) and the apparent Arrhenius parameters (E_a, ln A) determined by the Arrhenius plots were twice as large as those determined without considering the contribution of $p(CO_2)_{SG}$. Despite the complex kinetic results, the coefficients (c, d) provided useful information for interpreting the specific features of the SR and PBR processes. In the modified, extended Arrhenius plot for SR, the d value was determined to be unity, implying the direct influence of the atmospheric CO_2 because of the direct contact of the reaction sites with the atmosphere. Simultaneously, the c value was also determined to be approximately unity, indicating that the effect of $p(CO_2)_{SG}$ is not negligible from the SR process. In comparison with SR, the coefficients (c, d) for PBR(n) were characterized by the increase in the c value and the decrease in the d value. The changes in the (c, d) values as the reaction step advanced from SR to PBR are reasonable because the PBR is the internal process where the surface product layer intervenes in the direct contact of the atmosphere and the reaction interface. Note that when the same calculation was applied to the IP process, we exactly obtained the values of (c, d) = (0, 1) because the evolution of CO_2 does not occur.

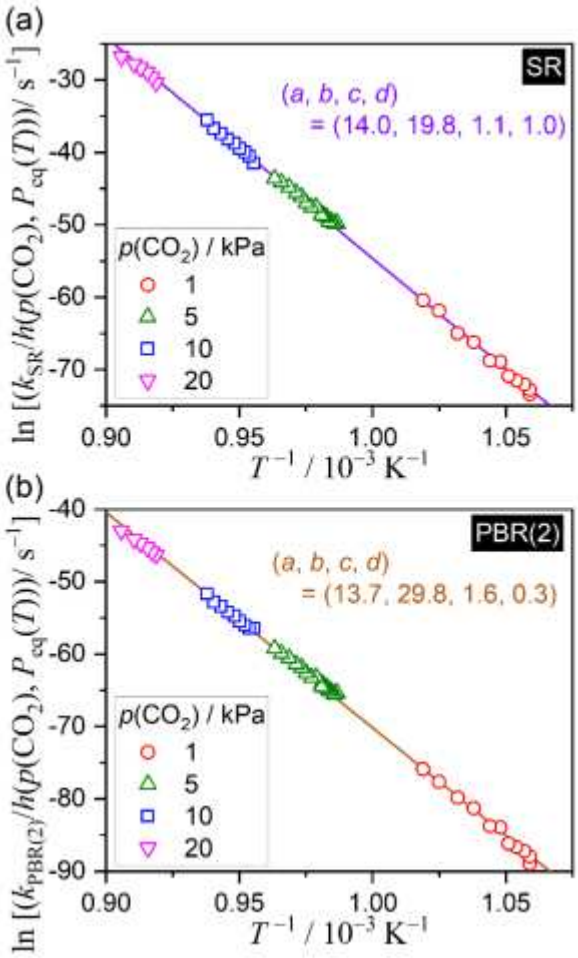

Figure 13. The extended Arrhenius plots over different temperatures and $p(CO_2)$ values, modified by considering the contributions of $p(CO_2)_{SG}$ and $p(CO_2)_{ATM}$ for the k values derived based on the IP– SR–PBR(2) model: (a) SR and (b) PBR(2) processes.

Table 5. Kinetic parameters determined by the modified extended Arrhenius plots considering the contributions of atmospheric and self-generated $p(CO_2)$

model	step	a	b	c	d	E_a/kJ mol^{-1}	ln[($A/h(p(CO_2), P_{eq}(T))$/s^{-1}]	$-\gamma$ [a]
IP–SR–PBR(2)	SR	13.97	19.78	1.08	1.00	2533 ± 12	250 ± 2	0.9995
	PBR(2)	13.70	29.77	1.62	0.32	2470 ± 13	227 ± 2	0.9994
IP–SR–PBR(3)	SR	14.25	21.66	1.35	1.00	2573 ± 12	254 ± 2	0.9995
	PBR(3)	13.72	31.17	1.96	0.32	2478 ± 13	227 ± 2	0.9995

[a] Correlation coefficient of the linear regression analysis for the extended Arrhenius plot.

4. Conclusions

Kinetic analysis of the thermal decomposition of $CaCO_3$ under carefully selected sampling and measurement conditions for reducing the negative effects of mass and heat transfer phenomena represented ideal results as a single-step kinetic process in views of the constancy of the isoconversional E_a values during the reaction ($E_a = 186.5 \pm 0.6$ kJ mol^{-1}) and the correspondence of the experimental master plot to the physico-geometrical reaction feature (R(1.39 ± 0.01)) with A value in the order of 107 s^{-1}. The presence of CO_2 in the reaction environment changed the kinetic behavior substantially, resulting in a significant retardation effect. Under isothermal conditions, the appearance of IP and subsequent sigmoidal mass loss behavior, in addition to the systematic shift of the reaction to the higher temperature with increasing $p(CO_2)$, were observed, indicating changes in the physico-geometrical reaction mechanism by the effect of atmospheric CO_2. Individual linear correlations of the Arrhenius-type temperature dependency were observed for the reactions at each $p(CO_2)$ value when the IP and mass-loss processes were investigated using the conventional kinetic calculation methods without considering the effect of $p(CO_2)$. The resulting apparent E_a values increased systematically with increasing $p(CO_2)$ and reached unexpectedly large values of $E_{a,IP} = 3253 \pm 571$ kJ mol^{-1} and $E_a = 1421 \pm 15$ kJ mol^{-1} for the IP and mass-loss processes at $p(CO_2) = 20$ kPa, respectively. The universal kinetic descriptions of these kinetic processes over different temperatures and $p(CO_2)$ values were examined by introducing AF composed of $p(CO_2)$ and $P_{eq}(T)$. An analytical form of AF with variable exponents (a, b) (eq. (14)) was derived based on the consecutive elementary steps in surface nucleation and interface reaction with rate-limiting step and steady-state assumptions. The introduction of the AF in the conventional kinetic equations realized the linear correlations of the Arrhenius-type plot for the IP process and the isoconversional plots for the mass-loss process including all data points recorded across different temperatures and $p(CO_2)$ values, by optimizing the exponents (a, b) in the AF. The kinetics of IP and mass-loss processes were characterized universally by $E_{a,IP} = 1752 \pm 10$ kJ mol^{-1} with (a, b) = (9.50, 1) and average E_a = 1023 ± 6 kJ mol^{-1} with average (a, b) = (5.17 ± 0.12, 4.39 ± 0.25), respectively. Furthermore, the rate behavior of the mass-loss process at a constant temperature was described universally by the extended experimental master plot considering the AF, exhibiting the initial acceleration and subsequent deceleration features with the maximum rate midway through the mass-loss process. Therefore, the overall process under isothermal conditions was successfully described by the physico-geometrical consecutive IP–SR–PBR(n) models with $n = 2$ or 3, irrespective of $p(CO_2)$. The kinetics of each physico-geometrical reaction step were universally described over different temperatures and $p(CO_2)$ values by examining the temperature dependence of the k_{IP}, k_{SR}, and $k_{PBR(n)}$ values using the extended Arrhenius plots with the AF. As a result, the universal kinetic features of the physico-geometrical consecutive process were characterized by systematic decreases in the exponent a and apparent E_a values as the physico-geometrical reaction step advanced from IP to PBR(n) via SR (Table 4). The universal kinetic plots for the mass-loss process were further improved by considering the contribution of self-generated CO_2 with empirical expressions of the effective $p(CO_2)$ as the sum of the contributions of self-generated and atmospheric $p(CO_2)$ (eqs. (19) and (20)). The ideal linear correlations of the extended Friedman plots for the mass-loss process and the extended Arrhenius plots for SR and PBR(n) processes were achieved by optimizing the contributions (c, d) of the self-generated and atmospheric $p(CO_2)$, respectively, together with exponents (a, b) in the AF. In the modified, extended Friedman plots, the constant c value during the reaction and the decrease in the d value in the final stage of the reaction were indicative of the possible contribution of the self-generated $p(CO_2)$ and the decrease in the contribution of the atmospheric $p(CO_2)$ in the latter stage of the

reaction, respectively. The extended Arrhenius plots for the SR and PBR(n) processes showed more clearly the changes in the contributions of the self-generated and atmospheric $p(CO_2)$, characterized by the increase in the c value and decrease in the d value as the physico-geometrical reaction step advanced from SR to PBR(n).

The kinetics of the thermal decomposition of $CaCO_3$ can be described universally over different temperatures and $p(CO_2)$ values by introducing the AF considering $p(CO_2)$ and $P_{eq}(T)$ values. The universal kinetic approach can be used as an empirical tool to parameterize the magnitude of the effect of $p(CO_2)$ on the kinetics via the exponents (a, b) in the AF. The universal kinetic description and parameterization of the effect of $p(CO_2)$ can be applied to each reaction step in the physico-geometrical consecutive reaction of IP–SR–PBR(n), enabling the detection of changes in the universal kinetics and the effect of $p(CO_2)$ as the reaction step advanced from IP to PBR(n) via SR. Using the proposed universal kinetic approach, possibility of estimating the effect of self-generated $p(CO_2)$ on the kinetics was also examined, obtaining a promising result.

ASSOCIATED CONTENT Supporting Information

The Supporting Information is available free of charge on the ACS Publications website at DOI: ????????.

S1. Sample characterization (Figures S1 and S2); S2. Kinetics of the thermal decomposition of $CaCO_3$ in a stream of dry N_2 (Figures S3 and S4); S3. Kinetics of the induction period at different $p(CO_2)$ values (Table S1, Figure S5); S4. Kinetics of the mass-loss process at different $p(CO_2)$ values (Figure S6, Table S2); and S5. Kinetic analysis based on the IP–SR–PBR model at different $p(CO_2)$ values (Figures S7– S11, Tables S3–S5).

AUTHOR INFORMATION

Corresponding Author

*Tel./fax: +81-82-424-7092. E-mail: nkoga@hiroshima-u.ac.jp

Notes

The authors declare no competing financial interest.

ACKNOWLEDGEMENTS

The present work was supported by JSPS KAKENHI Grant Numbers 17H00820, 19K03144, and 19K02708

References

1. Tegethoff, F. W., *Calcium Carbonate: From the Cretaceous Period into the 21st Century*; Springer: Basel, 2001.
2. Edwards, S. E. B.; Materić, V., Calcium Looping in Solar Power Generation Plants. *Sol. Energy* **2012**, *86*, 2494-2503.
3. Sakellariou, K. G.; Karagiannakis, G.; Criado, Y. A.; Konstandopoulos, A. G., Calcium Oxide Based Materials for Thermochemical Heat Storage in Concentrated Solar Power Plants. *Sol. Energy* **2015**, *122*, 215-230.
4. Fedunik-Hofman, L.; Bayon, A.; Hinkley, J.; Lipiński, W.; Donne, S. W., Friedman Method Kinetic Analysis of CaO-Based Sorbent for High-Temperature Thermochemical Energy Storage. *Chem. Eng. Sci.* **2019**, *200*, 236-247.
5. Benitez-Guerrero, M.; Valverde, J. M.; Perejón, A.; Sánchez Jiménez, P. E.; Pérez Maqueda, L. A., Low-Cost Ca-Based Composites Synthesized by Biotemplate Method for

Thermochemical Energy Storage of Concentrated Solar Power. *Appl. Energy* **2018**, *210*, 108-116.
6. Sánchez Jiménez, P. E.; Perejón, A.; Benítez Guerrero, M.; Valverde, J. M.; Ortiz, C.; Pérez Maqueda, L. A., High-Performance and Low-Cost Macroporous Calcium Oxide Based Materials for Thermochemical Energy Storage in Concentrated Solar Power Plants. *Appl. Energy* **2019**, *235*, 543-552.
7. Da, Y.; Xuan, Y.; Teng, L.; Zhang, K.; Liu, X.; Ding, Y., Calcium-Based Composites for Direct Solar-Thermal Conversion and Thermochemical Energy Storage. *Chem. Eng. J.* **2020**, *382*, 122815.
8. Sarrión, B.; Perejón, A.; Sánchez-Jiménez, P. E.; Amghar, N.; Chacartegui, R.; Manuel Valverde, J.; Pérez-Maqueda, L. A., Calcination under Low CO_2 Pressure Enhances the Calcium Looping Performance of Limestone for Thermochemical Energy Storage. *Chem. Eng. J.* **2020**, 127922.
9. Sarrión, B.; Perejón, A.; Sánchez-Jiménez, P. E.; Pérez-Maqueda, L. A.; Valverde, J. M., Role of Calcium Looping Conditions on the Performance of Natural and Synthetic Ca-Based Materials for Energy Storage. *J. CO_2 Util.* **2018**, *28*, 374-384.
10. Arcenegui Troya, J. J.; Moreno, V.; Sánchez-Jiménez, P. E.; Perejón, A.; Valverde, J. M.; PérezMaqueda, L. A., Effect of Steam Injection During Carbonation on the Multicyclic Performance of Limestone ($CaCO_3$) under Different Calcium Looping Conditions: A Comparative Study. *ACS Sustain. Chem. Eng.* **2022**, *10*, 850-859.
11. Arcenegui-Troya, J.; Sánchez-Jiménez, P. E.; Perejón, A.; Moreno, V.; Valverde, J. M.; PérezMaqueda, L. A., Kinetics and Cyclability of Limestone ($CaCO_3$) in Presence of Steam During Calcination in the CaL Scheme for Thermochemical Energy Storage. *Chem. Eng. J.* **2021**, *417*.
12. Arcenegui-Troya, J.; Sánchez-Jiménez, P. E.; Perejón, A.; Valverde, J. M.; Chacartegui, R.; Pérez-Maqueda, L. A., Calcium-Looping Performance of Biomineralized $CaCO_3$ for CO_2 Capture and Thermochemical Energy Storage. *Ind. Eng. Chem. Res.* **2020**, *59*, 12924-12933.
13. Chen, J.; Duan, L.; Sun, Z., Review on the Development of Sorbents for Calcium Looping. *Energy Fuels* **2020**, *34*, 7806-7836.
14. Nie, L.; Mu, Y.; Jin, J.; Chen, J.; Mi, J., Recent Developments and Consideration Issues in Solid Adsorbents for CO_2 Capture from Flue Gas. *Chin. J. Chem. Eng.* **2018**, *26*, 2303-2317.
15. Xu, Y.; Ding, H.; Luo, C.; Zheng, Y.; Zhang, Q.; Li, X.; Sun, J.; Zhang, L., Potential Synergy of Chlorine and Potassium and Sodium Elements in Carbonation Enhancement of CaO-Based Sorbents. *ACS Sustain. Chem. Eng.* **2018**, *6*, 11677-11684.
16. Erans, M.; Manovic, V.; Anthony, E. J., Calcium Looping Sorbents for CO_2 Capture. *Appl. Energy* **2016**, *180*, 722-742.
17. Nawar, A.; Ghaedi, H.; Ali, M.; Zhao, M.; Iqbal, N.; Khan, R., Recycling Waste-Derived Marble Powder for CO_2 Capture. *Process Saf. Environ. Prot.* **2019**, *132*, 214-225.
18. Fedunik, H.; Bayon; Donne, Comparative Kinetic Analysis of $CaCO_3$/CaO Reaction System for Energy Storage and Carbon Capture. *Appl. Sci.* **2019**, *9*, 4601.
19. Scaltsoyiannes, A. A.; Lemonidou, A. A., On the Factors Affecting the Deactivation of Limestone under Calcium Looping Conditions: A New Comprehensive Model. *Chem. Eng. Sci.* **2021**, *243*.
20. Berger, E. E., Effect of Steam on the Decomposition of Limestone. *Ind. Eng. Chem.* **1927**, *19*, 594-596.
21. Zawadzki, J.; Bretsznajder, S., Some Remarks on the Mechanism of Reactions of the Type: Solid=Solid + Gas. *Trans. Faraday Soc.* **1938**, *34*, 951-959.

22. Hyatt, E. P.; Cutler, I. B.; Wadsworth, M. E., Calcium Carbonate Decomposition in Carbon Dioxide Atmosphere. *J. Am. Ceram. Soc.* **1958**, *41*, 70-74.
23. Ingraham, T. R.; Marier, P., Kinetic Studies on the Thermal Decomposition of Calcium Carbonate. *Can. J. Chem. Eng.* **1963**, *41*, 170-173.
24. Searcy, A. W.; Beruto, D., Kinetics of Endothermic Decomposition Reactions. 2. Effects of the Solid and Gaseous Products. *J. Phys. Chem.* **1978**, *82*, 163-167.
25. Criado, J.; González, M.; Málek, J.; Ortega, A., The Effect of the CO_2 Pressure on the Thermal Decomposition Kinetics of Calcium Carbonate. *Thermochim. Acta* **1995**, *254*, 121-127.
26. Wang, Y.; Thomson, W. J., The Effects of Steam and Carbon Dioxide on Calcite Decomposition Using Dynamic X-Ray Diffraction. *Chem. Eng. Sci.* **1995**, *50*, 1373-1382.
27. Khinast, J.; Krammer, G. F.; Brunner, C.; Staudinger, G., Decomposition of Limestone: The Influence of CO_2 and Particle Size on the Reaction Rate. *Chem. Eng. Sci.* **1996**, *51*, 623-634.
28. Bouineau, V.; Pijolat, M.; Soustelle, M., Characterisation of the Chemical Reactivity of a $CaCO_3$ Powder for Its Decomposition. *J. Europ. Ceram. Soc.* **1998**, *18*, 1319-1324.
29. Koga, N.; Criado, J. M., The Influence of Mass Transfer Phenomena on the Kinetic Analysis for the Thermal Decomposition of Calcium Carbonate by Constant Rate Thermal Analysis (CRTA) under Vacuum. *Int. J. Chem. Kinet.* **1998**, *30*, 737-744.
30. Fujimoto, S.; Hanaoka, T.; Taniguchi, H.; Kuramoto, K.; Matsumura, Y.; Lin, S.-Y.; Minowa, T., A Kinetic Study of the Decomposition of $CaCO_3$ at High CO_2 Partial Pressure for the Regeneration of a CO_2 Sorbent. *J. Chem. Eng. Jpn.* **2006**, *39*, 1191-1194.
31. Koga, N., Ozawa's Kinetic Method for Analyzing Thermoanalytical Curves. *J. Therm. Anal. Calorim.* **2013**, *113*, 1527-1541.
32. Koga, N., Physico-Geometric Approach to the Kinetics of Overlapping Solid-State Reactions. In *Handbook of Thermal Analysis and Calorimetry*, 2nd ed.; Vyazovkin, S.; Koga, N.; Schick, C., Eds. Elsevier: Amsterdam, 2018; Vol. 6, pp 213-251.
33. Koga, N.; Šesták, J.; Simon, P., Some Fundamental and Historical Aspects of Phenomenological Kinetics in the Solid State Studied by Thermal Analysis. In *Thermal Analysis of Micro, Nano- and NonCrystalline Materials*, Šesták, J.; Simon, P., Eds. Springer: 2013; pp 1-28.
34. Galwey, A. K.; Brown, M. E., *Thermal Decomposition of Ionic Solids*; Elsevier: Amsterdam, 1999.
35. Galwey, A. K., Structure and Order in Thermal Dehydrations of Crystalline Solids. *Thermochim. Acta* **2000**, *355*, 181-238.
36. Koga, N.; Tanaka, H., A Physico-Geometric Approach to the Kinetics of Solid-State Reactions as Exemplified by the Thermal Dehydration and Decomposition of Inorganic Solids. *Thermochim. Acta* **2002**, *388*, 41-61.
37. Maciejewski, M.; Reller, A., How (Un)Reliable Are Kinetic Data of Reversible Solid-State Decomposition Processes? *Thermochim. Acta* **1987**, *110*, 145-152.
38. Vyazovkin, S.; Burnham, A. K.; Criado, J. M.; Pérez-Maqueda, L. A.; Popescu, C.; Sbirrazzuoli, N., ICTAC Kinetics Committee Recommendations for Performing Kinetic Computations on Thermal Analysis Data. *Thermochim. Acta* **2011**, *520*, 1-19.
39. Deutsch, M.; Birkelbach, F.; Knoll, C.; Harasek, M.; Werner, A.; Winter, F., An Extension of the NPK Method to Include the Pressure Dependency of Solid State Reactions. *Thermochim. Acta* **2017**, *654*, 168-178.
40. Vyazovkin, S., Kinetic Effects of Pressure on Decomposition of Solids. *Int. Rev. Phys. Chem.* **2020**, *39*, 35-66.
41. Benton, A. F.; Drake, L. C., Kinetics of Reaction and Adsorption in the System Silver—Oxygen. *J. Am. Chem. Soc.* **1934**, *56*, 255-263.

42. Reading, M.; Dollimore, D.; Whitehead, R., The Measurement of Meaningful Kinetic Parameters for Solid State Decomposition Reactions. *J. Therm. Anal.* **1991**, *37*, 2165-2188.
43. Barret, P., Expression théorique en Fonction de la Pression de la Loi de Vitesse de Croissance d'une Couche Non Protectrice Formée par Décomposition Thermique d'un Solide. *C. R. Acad. Sci. Paris, Serie C* **1968**, *266*, 856-859.
44. Mampel, K. L., Time Conversion Formulas for Heterogeneous Reactions at the Phase Boundaries of Solid Bodies, I: The Development of the Mathematical Method and the Derivation of Area Conversion Formulas. *Z. Phys. Chem., Abt. A* **1940**, *187*, 43-57
45. Favergeon, L.; Pijolat, M.; Soustelle, M., Surface Nucleation and Anisotropic Growth Models for Solid-State Reactions. *Thermochim. Acta* **2017**, *654*, 18-27.
46. Ogasawara, H.; Koga, N., Kinetic Modeling for Thermal Dehydration of Ferrous Oxalate Dihydrate Polymorphs: A Combined Model for Induction Period-Surface Reaction-Phase Boundary Reaction. *J. Phys. Chem. A* **2014**, *118*, 2401-2412.
47. Koga, N.; Favergeon, L.; Kodani, S., Impact of Atmospheric Water Vapor on the Thermal Decomposition of Calcium Hydroxide: A Universal Kinetic Approach to a Physico-Geometrical Consecutive Reaction in Solid-Gas Systems under Different Partial Pressures of Product Gas. *Phys. Chem. Chem. Phys.* **2019**, *21*, 11615-11632.
48. Fukuda, M.; Favergeon, L.; Koga, N., Universal Kinetic Description for Thermal Decomposition of Copper(II) Hydroxide over Different Water Vapor Pressures. *J. Phys. Chem. C* **2019**, *123*, 20903-20915.
49. Yamamoto, Y.; Favergeon, L.; Koga, N., Thermal Dehydration of Lithium Sulfate Monohydrate Revisited with Universal Kinetic Description over Different Temperatures and Atmospheric Water Vapor Pressures. *J. Phys. Chem. C* **2020**, *124*, 11960-11976.
50. Kodani, S.; Iwasaki, S.; Favergeon, L.; Koga, N., Revealing the Effect of Water Vapor Pressure on the Kinetics of Thermal Decomposition of Magnesium Hydroxide. *Phys. Chem. Chem. Phys.* **2020**, *22*, 13637-13649.
51. Koga, N.; Sakai, Y.; Fukuda, M.; Hara, D.; Tanaka, Y.; Favergeon, L., Universal Kinetics of the Thermal Decomposition of Synthetic Smithsonite over Different Atmospheric Conditions. *J. Phys. Chem. C* **2021**, *125*, 1384-1402.
52. Sakai, Y.; Iwasaki, S.; Kikuchi, S.; Koga, N., Influence of Atmospheric CO2 on the Thermal Decomposition of Perlite Concrete. *J. Therm. Anal. Calorim.* **2021**.
53. Sakai, Y.; Koga, N., Kinetics of Component Reactions in Calcium Looping Appeared During the Multistep Thermal Decomposition of Portland Cement under Various Atmospheric Conditions. *Chem. Eng. J.* **2022**, *428*, 131197.
54. Markgraf, S. A.; Reeder, R. J., High-Temperature Structure Refinements of Calcite and Magnesite. *Am. Mineral* **1985**, *70*, 590-600.
55. Brunauer, S.; Emmett, P. H.; Teller, E., Adsorption of Gases in Multimolecular Layers. *J. Am. Chem. Soc.* **1938**, *60*, 309-319.
56. Toft Sorensen, O. T.; Rouquerol, J., *Sample Controlled Thermal Analysis*; Kluwer: Dordrecht, 2003.
57. Criado, J. M.; Perez-Maqueda, L. A.; Koga, N., Sample Controlled Thermal Analysis (SCTA) as a Promising Tool for Kinetic Characterization of Solid-State Reaction and Controlled Material Synthesis. In *Thermal Physics and Thermal Analysis*, Šesták, J.; Hubík, P.; Mareš, J. J., Eds. Springer Nature: Switzerland, 2017; pp 11-43.
58. Vyazovkin, S.; Chrissafis, K.; Di Lorenzo, M. L.; Koga, N.; Pijolat, M.; Roduit, B.; Sbirrazzuoli, N.; Suñol, J. J., ICTAC Kinetics Committee Recommendations for Collecting Experimental Thermal Analysis Data for Kinetic Computations. *Thermochim. Acta* **2014**, *590*, 1-23.

59. Friedman, H. L., Kinetics of Thermal Degradation of Char-Forming Plastics from Thermogravimetry: Application to a Phenolic Plastic. *J. Polym. Sci., Part C* **1964**, *6*, 183-195.
60. Ozawa, T., Kinetic Analysis of Derivative Curves in Thermal Analysis. *J. Therm. Anal.* **1970**, *2*, 301-324.
61. Ozawa, T., Applicability of Friedman Plot. *J. Therm. Anal.* **1986**, *31*, 547-551.
62. Málek, J., The Kinetic Analysis of Non-Isothermal Data. *Thermochim. Acta* **1992**, *200*, 257-269.
63. Koga, N., Kinetic Analysis of Thermoanalytical Data by Extrapolating to Infinite Temperature. *Thermochim. Acta* **1995**, *258*, 145-159.
64. Gotor, F. J.; Criado, J. M.; Málek, J.; Koga, N., Kinetic Analysis of Solid-State Reactions: The Universality of Master Plots for Analyzing Isothermal and Nonisothermal Experiments. *J. Phys. Chem. A* **2000**, *104*, 10777-10782.
65. Criado, J. M.; Perez-Maqueda, L. A.; Gotor, F. J.; Málek, J.; Koga, N., A Unified Theory for the Kinetic Analysis of Solid State Reactions under Any Thermal Pathway. *J. Therm. Anal. Calorim.* **2003**, *72*, 901-906.
66. Ozawa, T., A New Method of Analyzing Thermogravimetric Data. *Bull. Chem. Soc. Jpn.* **1965**, *38*, 1881-1886.
67. Ozawa, T., Non-Isothermal Kinetics and Generalized Time. *Thermochim. Acta* **1986**, *100*, 109- 118.
68. Šesták, J.; Berggren, G., Study of the Kinetics of the Mechanism of Solid-State Reactions at Increasing Temperatures. *Thermochim. Acta* **1971**, *3*, 1-12.
69. Šesták, J., Diagnostic Limits of Phenomenological Kinetic Models Introducing the Accommodation Function. *J. Therm. Anal.* **1990**, *36*, 1997-2007.
70. Šesták, J., Rationale and Fallacy of Thermoanalytical Kinetic Patterns. *J. Therm. Anal. Calorim.* **2011**, *110*, 5-16.
71. Hansen, L. D.; Eatough, D. J.; Lewis, E. A.; Bergstrom, R. G.; Degraft-Johnson, D.; CassidyThompson, K., Shelf-Life Prediction from Induction Period Calorimetric Measurements on Materials Undergoing Autocatalytic Decomposition. *Can. J. Chem.* **1990**, *68*, 2111-2114.
72. Šimon, P., Induction Periods. *J. Therm. Anal. Calorim.* **2006**, *84*, 263-270.
73. Koga, N.; Kimizu, T., Thermal Decomposition of Indium(III) Hydroxide Prepared by the Microwave-Assisted Hydrothermal Method. *Journal of the American Ceramic Society* **2008**, *91*, 4052- 4058.
74. Kimura, T.; Koga, N., Thermal Dehydration of Monohydrocalcite: Overall Kinetics and Physico-Geometrical Mechanisms. *J. Phys. Chem. A* **2011**, *115*, 10491-501.
75. Fukuda, M.; Koga, N., Kinetics and Mechanisms of the Thermal Decomposition of Copper(II) Hydroxide: A Consecutive Process Comprising Induction Period, Surface Reaction, and Phase Boundary-Controlled Reaction. *J Phys Chem C* **2018**, *122*, 12869-12879.
76. Kröger, F. A., *The Chemistry of Imperfect Crystals: Vol.2, Imperfection Chemistry of Crystalline Solids*; North-Holland Publishing Company: Amsterdam, 1974.
77. Yokokawa, H.; Yamauchi, S.; Matsumoto, T., The Thermodynamic Database MALT. *Calphad* **1999**, *23*, 357-364.
78. Yokokawa, H.; Yamauchi, S.; Matsumoto, T., Thermodynamic Database MALT for Windows with gem and CHD. *Calphad* **2002**, *26*, 155-166.
79. Liavitskaya, T.; Vyazovkin, S., Discovering the Kinetics of Thermal Decomposition During Continuous Cooling. *Phys. Chem. Chem. Phys.* **2016**, *18*, 32021-32030.

80. Liavitskaya, T.; Vyazovkin, S., Delving into the Kinetics of Reversible Thermal Decomposition of Solids Measured on Heating and Cooling. *J. Phys. Chem. C* **2017**, *121*, 15392-15401.
81. Preturlan, J. G. D.; Vieille, L.; Quiligotti, S.; Favergeon, L., Kinetics and Mechanism of the Dehydration of Calcium Sulfate Dihydrate: A Comprehensive Approach for Studying the Dehydration of Ionic Hydrates under Controlled Temperature and Water Vapor Pressure. *J. Phys. Chem. C* **2020**, *124*, 26352-26367.
82. Serris, E.; Favergeon, L.; Pijolat, M.; Soustelle, M.; Nortier, P.; Gärtner, R. S.; Chopin, T.; Habib, Z., Study of the Hydration of CaO Powder by Gas–Solid Reaction. *Cem. Concr. Res.* **2011**, *41*, 1078-1084.
83. Rouchon, L.; Favergeon, L.; Pijolat, M., New Kinetic Model for the Rapid Step of Calcium Oxide Carbonation by Carbon Dioxide. *J. Therm. Anal. Calorim.* **2013**, *116*, 1181-1188.